Journal of King Saud University – Engineering Sciences (2026) 38:42
https://doi.org/10.1007/s44444-026-00115-0

RESEARCH

Systematic numerical analysis of thermal and hydraulic performance of nanofluids in double-tube heat exchangers

Olusegun Ilori[1] · Stephanie Inoma[1] · Rasheed Ayoola[1] · Joseph Orisaleye[1] · Anthony Ogunmefun[2]

Received: 29 December 2025 / Accepted: 7 June 2026

Abstract

Heat exchangers are central to thermal management in industrial, energy, and HVAC systems, motivating continued interest in advanced working fluids that enhance thermal performance. This study presents a computational investigation of the thermo-hydraulic performance of three nanofluids (MWCNT, SiO_2, and ZnO) flowing through a double-tube heat exchanger under identical geometrical and boundary conditions. An experimentally validated CFD model is used to isolate the effects of flow rate, nanoparticle concentration, and operating temperature on heat-transfer enhancement and pressure drop. Relative to water, nanofluids enhance heat transfer rates by approximately 6–40%, with a pressure drop of 8–106%. Increasing the volumetric flow rate to 600 l/h and the nanoparticle concentration to 0.25% yields the most significant thermal enhancement among all nanofluids. However, thermo-hydraulic evaluation shows that maximum heat-transfer enhancement alone does not guarantee optimal performance. When thermal and hydraulic effects are combined using the performance evaluation criterion (PEC), SiO_2 at 0.25% concentration yields a thermo-hydraulic improvement of approximately 11% relative to water, whereas ZnO, despite enhanced heat-transfer performance, incurs substantially higher-pressure losses. At high operating temperatures, heat transfer is further intensified, with ZnO exhibiting the highest sensitivity to thermal loading. The results establish a controlled reference for nanofluid comparison and provide practical guidance for selecting working fluids for compact, high-efficiency heat exchangers in HVAC, energy recovery, and industrial thermal management applications.

Highlights

- A controlled CFD framework isolates the effects of nanofluid type, flow rate, and concentration.
- The model is experimentally validated, achieving high agreement with measured heat transfer data.
- Nanofluids enhance heat transfer by up to 40% but incur pressure-drop increases of up to 106%.
- Performance evaluation shows SiO_2 nanofluid provides the best overall thermohydraulic balance.
- Results demonstrate that maximum heat-transfer enhancement does not guarantee optimal performance.

Keywords Double tube heat exchangers · Nanofluids · Heat transfer enhancement · Nanofluid concentration · Thermohydraulic performance · PEC

✉ Olusegun Ilori
olusegun.ilori@bcu.ac.uk

Stephanie Inoma
inomastephanie@gmail.com

Rasheed Ayoola
rasheed.ayoola@mail.bcu.ac.uk

Joseph Orisaleye
joseph.orisaleye@bcu.ac.uk

Anthony Ogunmefun
OgunmefunOA@tut.ac.za

[1] School of Architecture, Built Environment, Computing, and Engineering, Birmingham City University, Birmingham, United Kingdom

[2] Department of Chemical, Metallurgical, and Materials, Tshwane University of Technology, Pretoria, South Africa

Published online: 22 June 2026

Abbreviations

CFD	Computational fluid dynamics
CuO	Cupric oxide
HVAC	Heating, ventilation and air conditioning
LES	Large eddy simulation
MWCNT	Multi-walled carbon nanotubes
PVDF	Polyvinylidene fluoride
SAS	Scale adaptive simulation
SiO_2	Silicon oxide
ZnO	Zinc oxide
RANS	Reynolds-Averaged Navier–Stokes
PEC	Performance Evaluation Criterion
Nu	Nusselt number
Pr	Prandtl number
Re	Reynolds number

Subscripts

bf	Base fluid (water)
nf	Nanofluid
np	Nanoparticle
w	Wall
wall	Wall surface
o	Outer-tube
0	Reference value
j	Phase index
in	Inlet
out	Outlet
avg	Average

Symbols

A	Heat transfer area, m^2
f	Friction factor
ρ	Density, kg/m^3
Ɛ	Turbulence dissipation rate, m^2/s^3
t	Time, s
μ	Dynamic viscosity, $Pa.s$
μ_t	Turbulent viscosity, $Pa.s$
v	Kinematic viscosity, m^2/s
h, HTC	Heat transfer coefficient, W/m^2K
q"	Heat flux, W/m^2
Q	Heat transfer rate, W
D	Inner tube diameter (Hydraulic diameter), m
P	Pressure, Pa
g	Gravitational acceleration, m/s^2
ϕ	Volume fraction of nanofluids
w	Mass fraction of nanofluids
$\dot{m}$	Mass flow rate, kg/s
ΔP	Pressure drop, Pa
U, u	Fluid velocity (m/s)
T	Temperature, K
T_{in}	Inner-tube inlet temperature, K
T_{out}	Inner-tube outlet temperature, K
C_p	Specific heat capacity, $J/kg.K$
ΔT	temperature difference, K
ΔT_{lm}	Log-mean temperature difference, K
q''/q_0''	Normalised heat flux
$\Delta P/\Delta P_0$	Normalised Pressure drop,
T_{wall}	Wall temperature, K
k, λ	thermal conductivity, $W/m.K$
k_t	Turbulent kinetic energy, m^2/s^2
L	Tube length, m
y^+	Dimensionless wall distance
τ_w	Wall shear stress, Pa
δ	Interfacial layer thickness, m
δ_t	Thermal boundary layer thickness, m
ψ	Particle sphericity

1 Introduction

Heat exchangers are utilised in various industrial applications to transfer heat between two or more fluids at different temperatures for heat recovery and reuse. Their primary goals are to transfer heat from a hotter fluid to a colder one, facilitating efficient thermal energy exchange. Heat exchangers are fundamental components in thermal management systems across HVAC, power generation, automotive, chemical processing, and renewable energy sectors. Their efficiency directly influences energy consumption, operational cost, system reliability, and overall sustainability, critical concerns for modern engineering applications. As global energy demand continues to rise, improving the thermal performance of heat exchangers has become a central objective for both researchers and industry practitioners, as it is essential to enhance energy efficiency, reduce operating costs, and meet sustainability standards. Among various heat exchanger configurations, the double-tube heat exchanger remains widely used due to its simplicity, compactness, and effectiveness in applications requiring controlled heat transfer between two fluids.

Heat exchanger technologies have undergone significant evolution in response to the growing demand for sustainability and energy efficiency in industrial and energy systems. Geometric developments in heat transfer and general heat exchanger performance by Yuan et al. (2024), Perumal et al. (2022), Zhu and Haglind (2020), Marzouk et al. (2023), Shirvan et al. (2019), Afshari et al. (2021), Ilori et al. (2018, 2021), and Sam Solomon et al. (2022) show that optimising baffles within systems for certain flow rates and operational conditions reveals the positive effect structural changes may have on thermal performance. To maximise heat exchanger layouts using experimental and Computational Fluid Dynamics (CFD) techniques, Yuan et al. (2024), Zhu and Haglind (2020), and Sam Solomon et al. (2022) employed

CFD simulations to gain a thorough understanding of complex flow dynamics. Sam Solomon et al. (2022) identified that the heat transfer rate ($\dot{Q}$) per unit pressure drop (ΔP) increased from 17% to 38%. Their top-level investigation into balancing pumping power with heat transfer efficiency guided the design of more effective heat exchangers.

To enhance heat transfer performance beyond what is achievable with conventional working fluids, nanofluids (engineered suspensions of nanoparticles in base liquids) have emerged as a promising solution. Numerous studies have demonstrated that nanofluids can significantly improve thermal conductivity, convective heat transfer, and temperature uniformity within heat exchangers. Research reports heat transfer efficiency gains of up to 56% using nanofluids (Moradi et al. 2019), and their advantages are particularly evident in compact and microchannel heat exchangers where conventional fluids often underperform (Ajeeb and Murshed 2022; Rasheed et al. 2021). Among the most commonly investigated nanoparticles are silicon oxide (SiO_2), zinc oxide (ZnO), and multi-walled carbon nanotubes (MWCNTs). MWCNTs are valued for their exceptionally high thermal conductivity and mechanical strength, SiO_2 offers favourable heat transfer characteristics at relatively low cost, and ZnO is widely recognised for its stability and strong thermal performance (Ajeeb and Murshed 2022).

Recent state-of-the-art reviews have synthesised the broad landscape of nanofluid heat transfer, highlighting critical parameters such as thermal conductivity, viscosity, and nanoparticle dispersion methods. Notably, Chauhan and Kumar (2018) conducted a comprehensive review of nanofluid flow through microchannels, examining both heat transfer enhancement and ΔP. Their findings confirm that metallic oxide nanofluids, particularly CuO-water at 2 vol% and Reynolds number (Re) = 100, deliver substantial thermal performance improvements with only modest increases in friction factor, making them promising candidates for compact, high-efficiency heat exchanger designs. Alongside this, Islam et al. (2024) provided CFD-based insights into hybrid nanofluids in geometrically enhanced domains, demonstrating the synergistic benefits of combining nanoparticle composition with structural modifications. Similarly, studies by Ahmadi and Toghraie (2022), Mustakim et al. (2024) and Ahamed et al. (2024) investigated corrugated and baffled geometries paired with hybrid nanofluids, reporting performance enhancements exceeding 60% in Nusselt number (Nu) and significant increases in heat transfer coefficient (HTC), particularly at lower Re.

Islam et al. (2024) demonstrated that helical pipes with circular, triangular, and square jackets, when coupled with Al_2O_3, CuO, or an Al_2O_3/Cu hybrid nanofluid, can achieve up to a 60% improvement in heat transfer performance. Their results highlight the synergistic effect of the hybrid nanofluid composition and the enhanced geometric design, which promote turbulence generation and increase energy efficiency, albeit at higher ΔPs and friction factors. These findings indicate that hybrid nanofluids in modified geometries are well suited for applications requiring superior heat dissipation. Similarly, Mustakim et al. (2024) evaluated helically corrugated pipes with modified inlet shapes and varied corrugation pitches using single and hybrid nanofluids under turbulent conditions. Incorporating a 1% Al_2O_3/Cu hybrid nanofluid in the optimised configuration yielded a 29.2% increase in the HTC and a 24.3% rise in the Nu compared with base fluids. This study further confirms that corrugated geometries combined with hybrid nanofluids provide substantial thermal enhancement, particularly at lower Re, supporting their suitability for compact, high-efficiency heat exchanger applications.

Building on this, Ahamed et al. (2024) conducted a computational study on a curved trapezoidal-corrugated channel with E-shaped baffles, using hybrid nanofluids such as TiO_2–SiO_2 in a water–ethylene glycol base. Their results showed a 62% increase in the Nu and a 36.49% rise in PEC, with blockage ratio, nanoparticle composition, and baffle geometry all exerting significant influence on thermal performance. These findings demonstrate that hybrid nanofluids, when combined with structural optimisation, can outperform both smooth and conventionally corrugated configurations. Similar studies by Ahmad et al. (2023) and Islam et al. (2024) confirm that deploying hybrid nanofluids in enhanced geometries, such as corrugations, coils, and baffles, promotes higher turbulence, improved mixing, and overall greater thermal performance (PEC > 1). However, these works also highlight the associated increase in ΔP, reinforcing the observations of Qasim et al. (2020) and Prasad et al. (2022) regarding the need to balance heat transfer gains with energy costs. Meanwhile, Gabir and Alkhafaji (2021) and Vidhya et al. (2022) show that hybrid nanofluids such as Al_2O_3–MWCNT and Cu–TiO_2 can deliver substantial performance improvements with minimal additional pumping power, suggesting their suitability for next-generation compact heat exchangers. Recent studies have further examined the physical mechanisms governing nanofluid heat-transfer enhancement in internal flows, highlighting the roles of nanoparticle dispersion, Brownian motion, and turbulence–particle interactions in modifying thermal transport behaviour (Buongiorno 2006; Maghrabie et al. 2021; Maghrabie and Mousa 2022).

While extensive research has investigated nanofluids and hybrid nanofluids in heat exchangers, often within modified geometries such as corrugated, coiled, or baffled systems, a critical limitation remains: the lack of consistent comparisons across different nanoparticle types. In many previous studies, variations in geometry, operating conditions, or

modelling approaches make it difficult to isolate the intrinsic influence of nanofluid composition, concentration, and thermophysical properties on thermo-hydraulic performance. While many studies focus on a single nanofluid, there is a lack of a systematic comparison of morphologically distinct particles (tubular vs spherical) under identical transitional-to-turbulent flow conditions. To address this limitation, the present study adopts a controlled-comparison framework in which water-based nanofluids comprising MWCNT, SiO_2, and ZnO are evaluated using an experimentally validated CFD model under identical geometry and boundary conditions in a double-tube heat exchanger. This approach enables direct attribution of performance differences to fluid-specific properties, reducing confounding effects and providing a more physically consistent basis for assessing the trade-off between heat transfer enhancement and pressure drop penalty. The findings offer practical guidance for selecting nanofluids for compact, energy-efficient HVAC, industrial, and energy-system heat exchangers.

2 Methodology and methods

This study investigates the heat transfer performance of water-based nanofluids consisting of MWCNT, ZnO, and SiO_2 flowing through the inner tube of a double-tube heat exchanger. The CFD simulation is conducted in ANSYS Fluent to evaluate the thermo-hydraulic behaviour of nanofluids in a double-tube heat exchanger across varying flow rates, nanoparticle concentrations, and operating temperatures.

2.1 Model set up and assumptions

This study is based on the experimental work of Moradi et al. (2019), from which the geometry, boundary conditions, initial conditions, and CFD model validation are derived. The geometry is a double-tube heat exchanger, arranged in a counterflow configuration as shown in Fig. 1. It consists of two concentric cylindrical tubes that form the computational domain, which was discretised to accurately represent the physical system. The study involves two separate analyses: validation and extended CFD cases, as shown in Table 1. Hot fluid enters the inner tube (water or water-based nanofluid - MWCNT, ZnO, and SiO_2). Water enters the outer tube at 15 °C and 300 l/h, and is heated by the fluid in the inner tube for both validation and extended simulation cases.

2.2 Nanofluids specification

The three water-based nanofluids, including MWCNT, ZnO, and SiO_2, were selected due to their high thermal conductivity and demonstrated ability to enhance heat transfer in heat exchanger applications. The heat transfer efficiency of nanofluids depends strongly on their thermophysical

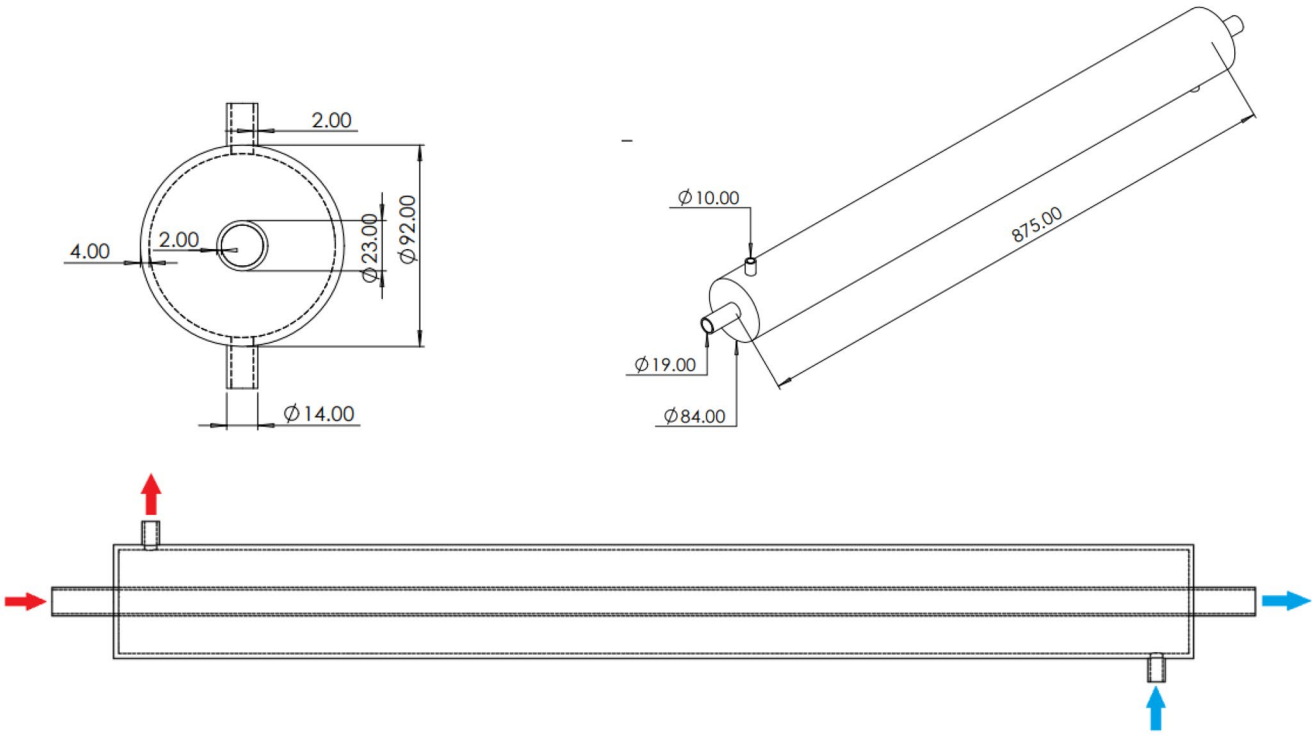

Fig. 1 Geometric dimensions of the Double-tube exchanger

Table 1 Operating and boundary conditions

Geometry	Parameters
Outer tube (cold fluid) Material: Polyvinylidene fluoride (white)	Validation and Extended CFD cases (Moradi et al. 2019). Flow rate: 300 l/h Temperature: 15 °C Fluid: Water
Inner tube (hot fluid) Material: Copper	Validation cases (Moradi et al. 2019). Flow rate: 100–300 l/h, Temperature: 50 °C Fluid = Water Extended CFD Cases. Flow rate: 100 l/h − 600 l/h Temperature: 40 °C − 70 °C Fluid: Water, MWCNT, ZnO, and SiO_2 Nanofluid mass concentration: 0.04%, 0.17%, and 0.25%

properties, including thermal conductivity, specific heat, viscosity, and density. Adjusting nanoparticle concentration helps identify the optimal balance between improved heat conduction and the accompanying increase in viscosity. All relevant thermophysical properties were treated as temperature-dependent and calculated using empirical correlations (Eqs. 1–4) adapted from Pak and Cho (1998), Buongiorno (2006), Khanafer and Vafai (2011), Gupta et al. (2016) and Moradi et al. (2019). This approach ensures that variations in nanofluid behaviour across the operational temperature range are accurately represented.

$$\rho_{nf} = \phi\rho_p + (1-\phi)\,\rho_{bf} \tag{1}$$

$$Cp_{nf} = \frac{\phi \times (\rho_p.\mathrm{Cp}_p) + (1-\phi) \times (\rho_{bf}.Cp_{bf})}{\rho_{nf}} \tag{2}$$

$$\mu_{nf} = (1+2.5\phi)\,\mu_{bf} \tag{3}$$

$$k_{nf} = k_{bf} \times \frac{k_p + 2k_{bf} + 2\phi\,(k_p - k_{bf})}{k_p + 2k_{bf} - \phi\,(k_p - k_{bf})} \tag{4}$$

$$\phi = \frac{w/\rho_p}{(w/\rho_p) + (1 - w/\rho_{bf})} \tag{5}$$

Where ρ = density; ϕ = volume fraction of nanoparticles; Cp = Specific heat capacity; μ = Dynamic viscosity; k = Thermal conductivity. Nanoparticle concentration was defined as a mass fraction (w = 0.04%, 0.17%, and 0.25%) and converted to volume fraction (ϕ) consistent with the thermophysical property correlations employed. The Einstein viscosity model (Eq. 3) provides a first-order approximation for dilute nanoparticle suspensions. Although originally derived for spherical particles, it is commonly applied to low-concentration nanofluids (≤1 vol%) where viscosity variations remain modest and effective-property modelling captures the dominant thermo-hydraulic behaviour (Einstein 1906; Pak and Cho 1998; Buongiorno 2006; Khanafer and Vafai 2011). Equation (4) is the classical Maxwell model for predicting the thermal conductivity of dilute nanoparticle suspensions. While more advanced correlations incorporate particle morphology, Brownian motion, and interfacial thermal resistance, these mechanisms become increasingly significant at higher nanoparticle loadings. For the dilute concentrations considered here (ϕ ≤0.25%), the Maxwell model provides a widely accepted and numerically stable approximation for CFD simulations of nanofluid heat transfer (Ajeeb and Murshed 2022; Porgar et al. 2023; Girhe et al. 2023).

In this study, nanofluids were modelled using a single-phase homogeneous approach, treating the base fluid and nanoparticles as a continuum with effective thermophysical properties. This formulation neglects slip velocity, sedimentation, and particle–particle interactions such as agglomeration. Given the low particle Stokes number expected in dilute suspensions, particle–fluid velocity slip remains negligible. However, for dilute nanofluids with relatively stable dispersion (ϕ ≤0.25%), single-phase effective-property models have been shown to provide reliable predictions of global heat-transfer behaviour in internal forced-convection flows (Buongiorno 2006; Albojamal and Vafai 2017; Ajeeb and Murshed 2022). The thermophysical properties were evaluated using established empirical correlations, including the Einstein model for viscosity and the Maxwell model for thermal conductivity. While more advanced formulations can account for particle morphology, Brownian motion, and interfacial effects, these mechanisms become increasingly significant at higher nanoparticle concentrations. For the dilute regime considered here, effective-property modelling captures the dominant thermo-hydraulic behaviour while maintaining numerical stability and computational efficiency. Accordingly, the present formulation applies to turbulent internal flows in double-tube heat exchangers operating within the investigated *Re* range and concentration limits (ϕ ≤0.25%), where nanoparticle slip and agglomeration effects remain limited, and continuum assumptions are valid. Nevertheless, the model does not explicitly account for particle–fluid interaction mechanisms, such as slip velocity, clustering, or turbulence modulation, and its applicability may therefore be reduced at higher concentrations or in systems with strong particle interactions.

Despite these limitations, the controlled-comparative framework adopted, in which all cases are evaluated under identical geometry, boundary conditions, and numerical settings, ensures that the reported trends in heat transfer, pressure drop, and thermo-hydraulic performance are internally consistent. While not intended as a universal predictive model, the observed trends are expected to remain qualitatively transferable to similar forced-convection systems, as

they are governed by the underlying interactions between *Re*, *Pr*, and effective thermal conductivity. The consistency of thermo-hydraulic behaviour across the investigated Reynolds number range further supports the robustness of the model within its defined applicability domain.

2.3 Governing equations

The CFD simulations are governed by the Navier–Stokes equations, which describe the fluid flow, and the energy equation, which models heat transfer between the tube wall and the working fluid. Together, these equations capture the coupled momentum and thermal transport processes within the heat exchanger. Solving them simultaneously, along with the corresponding Re and Nu formulations, yields the velocity and temperature fields required to characterise the system's thermo-hydraulic behaviour (ANSYS 2023; Estupiñán-Campos et al. 2024). The continuity, momentum, and energy equations are provided in Eqs. 6–8.

$$\frac{\partial \rho}{\partial t} + \nabla . \left(\rho \vec{V}\right) = Sm \tag{6}$$

$$\frac{\partial}{\partial t}\left(\rho \vec{V}\right) + \nabla . \left(\rho \vec{V}\vec{V}\right) = -\nabla P + \nabla . (\tau) + \rho \vec{g} + \vec{F} \tag{7}$$

$$\frac{\partial}{\partial t}(\rho E) + \nabla . \left[\vec{V} . (\rho E + P)\right] = \nabla . (k_{eff} \nabla T) + S_h \tag{8}$$

Where ρ=density; t=time; $\vec{V}$=velocity vector; Sm=mass source; $\rho\vec{V}$=momentum; $\rho\vec{V}\vec{V}$=advective momentum flux; ∇p=pressure gradient force; $\nabla . (\tau)$=viscous stress tensor; $\rho\vec{g}$=force due to gravity; F=external forces; ρE=thermal energy; $\vec{V} . (\rho E + P)$=convective energy flux; $k_{eff} = k_{nf} + \mu_t / Pr_t$=effective thermal conductivity (μ_t = turbulent viscosity and Pr_t=turbulent Prandtl number); S_h=source term.

2.4 Initial and boundary conditions

To solve the governing continuity, momentum, and energy equations described in Sect. 2.3, appropriate boundary conditions were applied to accurately simulate nanofluid flow and heat transfer at the inlets, outlets, and walls while ensuring numerical stability and physical consistency. The inlet conditions for the inner tube were defined as specified in Table 1. A uniform axial velocity profile was imposed based on the tube cross-sectional area. The outer-tube inlet was prescribed with a constant mass flow rate and a fixed inlet temperature. At both inner and outer outlets, a fully developed flow condition was assumed with a backflow condition normal to the boundary. The inner-tube wall, made of copper, was modelled as a conductive surface with material-specific thermal conductivity, and a no-slip boundary condition was imposed. The outer-tube wall was treated as thermally insulated (adiabatic) to prevent heat loss. The velocity and temperature fields were initialised using the inlet values. A transient solver with a time step of 0.01 s was employed to allow flow development and thermal stabilisation. Although a transient solver was employed, the simulations were advanced in time until a statistically steady thermal and hydrodynamic state was achieved. Convergence was assessed by monitoring residuals, mass imbalance, and key integral quantities, including outlet temperature, wall heat flux, and pressure drop. Once these quantities exhibited negligible temporal variation, the solution was considered converged. All reported results correspond to the final converged time step and therefore represent steady-state behaviour. The thermophysical properties of water and the nanoparticles are listed in Table 2. The nanofluid properties are calculated using the correlations described in Sect. 2.2. It should be noted that the thermophysical properties of the nanofluids were evaluated at the inlet temperature. In contrast, in the CFD simulations, these properties were implemented as temperature-dependent functions based on Eqs. (1–4) and updated according to the local temperature field. In Table 2, the intrinsic thermal conductivities of the nanoparticles were taken as 3000 W m^{-1} K^{-1} for MWCNT, 1.38 W m^{-1} K^{-1} for SiO_2, and 110.95 W m^{-1} K^{-1} for ZnO based on values reported in the literature (Moradi et al. 2019; Shahrul et al. 2016; Rasheed et al. 2021) for bulk or intrinsic material properties. Because the nanoparticle concentrations investigated are very low (<1%), the effective thermal conductivity of the nanofluids remains dominated by the base fluid.

Table 2 Thermophysical properties of water and MWCNT, SiO_2 and ZnO nanoparticles

Properties	Water	MWCNT	SiO_2	ZnO
Density, kg/m^3	997	2100	2500	5600
Specific heat capacity, J/kg.K	4182	702	710	502.7
Dynamic viscosity, Pa.s	5.47×10^{-4}		-	
Thermal conductivity, W/mK	0.60	3000	1.38	110.95

2.5 Flow development length estimation

To ensure accurate simulation of internal fluid dynamics, it is important to verify that the flow becomes fully developed within the computational domain. The flow development length depends on the Re, pipe diameter (D), and the flow regime. The parameters used in this analysis are defined in Eqs. 9–11, following the standard fluid-mechanics relations (White 2011).

$$Re = \frac{\rho \mathrm{UD}}{\mu} \tag{9}$$

where ρ is fluid density (kg/m^3), U is average velocity (m/s), and μ is dynamic viscosity (Pa.s). The velocity is obtained from the inlet volumetric flow (Q) and area (A) using:

$$U = \frac{\mathrm{Q}}{\mathrm{A}} \tag{10}$$

The Prandtl number (Pr) is defined as:

$$\mathrm{Pr} = \frac{C_p.\mu}{k} \tag{11}$$

Where k is the thermal conductivity of the fluid.

For an inner tube diameter of 19 mm and flow rates of 100–600 L/h (2.78×10^{-5} to 1.67×10^{-4} m^3/s), the corresponding bulk velocities range from approximately 0.10 m/s to 0.59 m/s, yielding Re between 3,400 (at 100 L/h) and 20,500 (at 600 L/h), indicating transitional to turbulent flow. The *Re* is reported based on inlet properties for consistency, while the simulation uses temperature-dependent properties locally. Nanofluids such as ZnO, with slightly higher density and lower viscosity, may yield marginally higher *Re* values. The entrance length L can be estimated using L=0.05*ReD* for laminar flow and L=10D for turbulent flow. The turbulent entrance-length approximation (L=10D) is a commonly adopted engineering estimate for fully turbulent internal pipe flow and has been widely reported in the classical fluid mechanics literature (White 2011). Although nanofluids are used, the nanoparticle concentrations remain within the dilute regime (ϕ ≤0.25%), where effective-property modelling is valid, and the hydrodynamic behaviour closely follows that of the base fluid. Given that the flow spans transitional to turbulent regimes, a conservative turbulent entrance-length approximation is adopted. For the present geometry (D = 19 mm, tube length = 1 m), this yields an entrance length of approximately 0.19 m, indicating that only a small portion of the domain is affected by flow development, while the majority of the tube operates under fully developed conditions.

2.6 Thermal and hydraulic performance evaluation

The thermal performance of the heat exchanger was evaluated using the tube-side area-weighted average wall heat flux, which provides a direct measure of the local convective heat-transfer intensity at the fluid–wall interface. The wall heat flux (q'') was extracted from the inner wetted surface of the inner tube, corresponding to the tube-side working fluid. Area-weighted averaging was employed to account for spatial variations along the heated surface. The heat transfer rate ($\dot{Q}$), average convective heat transfer coefficient (h), log-mean temperature difference (ΔT_{lm}), and the Nusselt number (Nu) are defined in Eqs. 12–15 (White 2011). Since all simulations were performed using an identical geometry and heated surface area (A), q'' is directly proportional to the $\dot{Q}$, which can be expressed as:

$$q'' = \frac{\dot{Q}}{A} \tag{12}$$

Since the same heated area is used for all cases, the ratio of $\dot{Q}$ equals the ratio of the corresponding q''. The h on the tube side was obtained from the q'' and ΔT_{lm} as:

$$h = \frac{q''}{\Delta T_{lm}} \tag{13}$$

Because a constant wall temperature boundary condition was imposed and the bulk fluid temperature varies axially along the tube, the ΔT_{lm} between the wall and the bulk fluid was used, defined as:

$$\Delta T_{lm} = \frac{(T_{wall} - T_{in}) - (T_{wall} - T_{out})}{\ln\left(\frac{T_{wall}-T_{in}}{T_{wall}-T_{out}}\right)} \tag{14}$$

Where T_{wall} is the area-weighted tube-side wall temperature, and T_{inlet} and T_{outlet} are the mass-flow-weighted average inlet and outlet bulk temperatures, respectively.

The corresponding *Nu* was evaluated using:

$$Nu = \frac{hD}{k} \tag{15}$$

where D is the tube diameter, and k is the thermal conductivity of the working fluid evaluated at the appropriate temperature and nanofluid concentration.

The ΔP was calculated as the area-weighted average static pressure difference between the inlet and outlet cross-sections of the inner tube. All ΔP values were extracted from converged steady-state solutions using identical numerical settings. For each operating condition investigated, a corresponding baseline simulation using water (base fluid) thermophysical properties was performed. The resulting reference pressure-drop (ΔP_0) and the reference heat flux (q_o'') values were used for normalisation. The thermo-hydraulic performance of the nanofluids was assessed using the performance evaluation criterion (PEC) (Webb and Eckert 1972; Webb 1981) to account for the combined effects of heat transfer enhancement and ΔP penalty. In this study, PEC is defined as:

$$PEC = \frac{(q''/q_0'')}{(\Delta P/\Delta P_0)^{1/3}} \tag{16}$$

The exponent $1/3$ accounts for the cubic relationship between pumping power and flow rate under turbulent or transitional flow conditions and is widely adopted in thermo-hydraulic performance assessments of heat exchangers (Webb and Eckert 1972; Webb 1981). Relative to the base fluid, a PEC value greater than unity indicates that the heat-transfer enhancement outweighs the hydraulic penalty, whereas a PEC < 1 implies that pressure losses dominate. Alternative exponent values would modify the relative weighting of the hydraulic penalty but would not significantly alter the comparative PEC trends among the nanofluids examined in this study.

2.7 Mesh sensitivity and Initial comparison

A mesh sensitivity analysis was conducted to ensure that the numerical predictions were independent of grid resolution. Inflation layers were applied near the tube and shell walls to adequately resolve near-wall velocity and thermal gradients. As shown in Fig. 2a, this meshing strategy enabled an accurate representation of boundary-layer development. Figure 2b presents the mesh convergence results, indicating that the predicted outlet velocity increased from approximately 0.257 m/s for a 350k-element mesh to 0.2655 m/s at 600k elements, corresponding to a change of about 3.3%. Beyond this point, further mesh refinement to 1.2 million, 2.4 million, and 4.8 million elements resulted in velocity variations of less than 0.5%, demonstrating mesh independence. Consequently, a mesh consisting of approximately 600,000 elements was selected as an optimal compromise between numerical accuracy and computational efficiency and was adopted for all subsequent simulations.

A transient solver was employed to capture the system's time-dependent behaviour and ensure that the solution reached thermal equilibrium before data extraction. Time-step sensitivity was assessed by monitoring residuals and the shell outlet velocity over a 10-second interval. Convergence of the governing Navier–Stokes equations was achieved at a time step of 0.01 seconds, which was therefore adopted for all subsequent simulations. The Y^+ values ranged from 30 to 100 across all cases, confirming the suitability of standard wall functions within the realizable k–ε turbulence model and ensuring accurate predictions of near-wall thermal and velocity fields (ANSYS 2023; Launder and Spalding 1974). Although slightly lower values were observed at reduced flow rates due to decreased wall shear, they remained within the logarithmic layer, appropriate for wall-function treatment, ensuring consistent near-wall modelling across the full range of operating conditions investigated.

After establishing mesh independence, a comparative assessment of turbulence models was performed by evaluating axial temperature variations along the heat exchanger. Four turbulence models: *k*–ω, *k*–ε, Scale-Adaptive Simulation (SAS), and Large Eddy Simulation (LES), were examined. The predicted temperature fields from each model were compared against analytically determined outer-tube outlet temperatures ($T_{o,out}$), calculated for the same outer-tube inlet conditions. The analytical outlet temperature was obtained using a steady-state energy balance, in which the exchanger duty was first evaluated for the inner-tube stream using mass and energy conservation, as defined by Eqs. 17 and 18 (White 2011). This comparison provided the basis for selecting the turbulence model that best reproduces the heat exchanger's thermal behaviour.

$$\dot{Q} = \dot{m} C_p \left(T_{out} - T_{in}\right) \tag{17}$$

The corresponding $T_{o,out}$ was calculated as:

$$T_{o,out} = T_{o,in} + \frac{\dot{Q}}{\dot{m}_o C_{p,o}} \tag{18}$$

where $\dot{m}_o$ and $C_{p,o}$ are the outer-tube mass flow rate and specific heat capacity, respectively, and $T_{o,in}$ is the outer-tube inlet temperature. The $\dot{m}_o = \rho_o \dot{V}_o$, where ρ_o and $\dot{V}_o$ are the density of the outer-tube working fluid and volumetric flow rate, respectively.

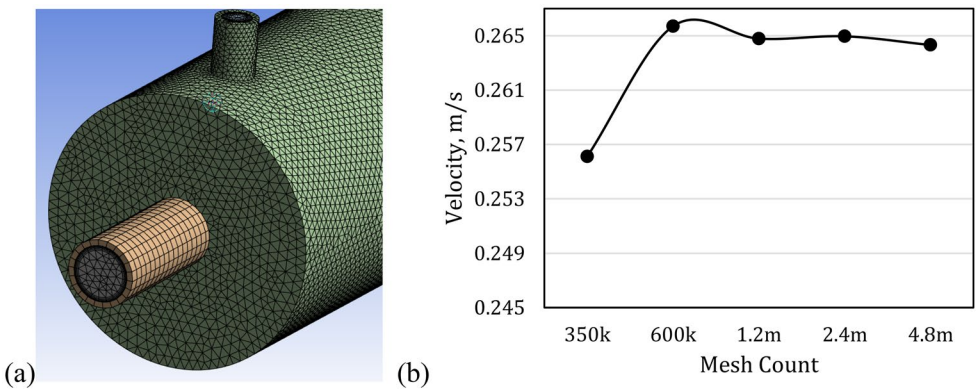

Fig. 2 Mesh convergence (**a**) inflation layer at tube inlet (**b**) mesh convergence plot

Figure 3 compares the temperature profiles along the heat exchanger for four turbulence models with the analytical solution. All models match the analytical inlet temperature (14 °C), but differences emerge as the flow develops. In the first 30 cm, the k–ε model shows the fastest temperature rise among the RANS models due to its tendency to overpredict turbulent mixing in transitional regions. The k–ω model predicts the lowest temperatures, reflecting its reduced turbulent diffusivity, while SAS and LES initially remain closer to k–ω as turbulence structures have not yet fully developed. Between 30 and 60 cm, the models diverge significantly. SAS and LES predict higher temperatures, indicating stronger mixing and more realistic turbulent heat transfer. LES performs best, resolving large-scale turbulent eddies responsible for energy transport. In contrast, both RANS models underpredict mixing, with the k–ω model exhibiting the largest deviation. Toward the outlet, SAS and LES converge toward the analytical temperature (34 °C), whereas k–ε and k–ω remain lower due to eddy-viscosity limitations.

To quantify the deviation between turbulence closures, the outer-tube outlet temperature predicted by the realizable k–ε model was compared with higher-fidelity LES and SAS results under identical boundary conditions. Across the investigated axial locations, the maximum deviation in outlet temperature between the realizable k–ε model and LES was within approximately 5–7%, while the corresponding deviation relative to SAS remained below 6%. These differences fall within the typical uncertainty range reported for RANS-based simulations of internal forced-convection heat transfer and are comparable to the experimental–numerical deviation observed during model validation. Given this level of agreement, deviations below 8% were considered acceptable for the present parametric study, particularly considering the substantial computational cost associated with LES and SAS approaches. Eddy-viscosity RANS models such as the realizable k–ε formulation are known to exhibit reduced predictive fidelity in transitional regimes due to their isotropic turbulence assumptions (Wilcox 2006).

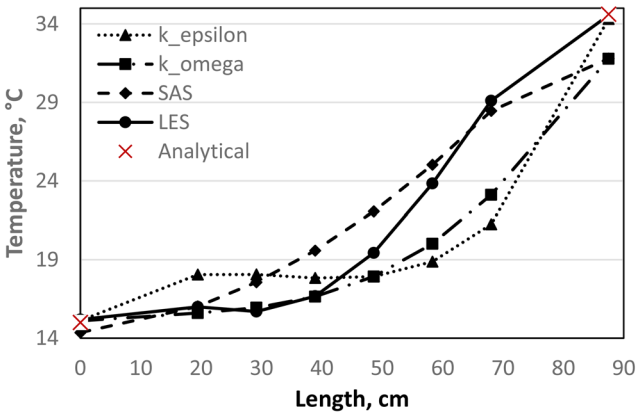

Fig. 3 Analytical model and turbulence models: k–ε, k–ω, SAS, and LES

Nevertheless, numerous CFD validation studies have shown that RANS models can reproduce global heat-transfer trends, with deviations typically within 5–10% relative to higher-fidelity simulations or experimental data, making them suitable for engineering parametric analyses (Kadivar et al. 2023). Based on this level of quantitative agreement and the associated computational constraints, the realizable k–ε model coupled with standard wall functions was selected for the remaining simulation cases. The turbulence-model comparison presented here focuses on global thermal behaviour using axial temperature distributions and outlet temperatures. While higher-fidelity models such as LES and SAS can provide more detailed local velocity and temperature structures, their significantly higher computational cost makes them impractical for the extensive parametric simulations performed in this study. This choice provides a pragmatic balance between predictive accuracy, numerical robustness, and computational efficiency while ensuring consistent treatment across the full parametric range investigated.

3 Model validation and uncertainty

3.1 Thermal and hydraulic validation

Figure 4 shows thermal and hydraulic validation of the numerical results. Figure 4a compares the experimentally measured and CFD-predicted h for water and MWCNT nanofluids (0.04% and 0.25%) under baseline conditions, as reported by Moradi et al. (2019). The h increases monotonically with flow rate for all fluids, rising from approximately 850–1150 W/m^2 K at 100 L/h to 1700–2400 W/m^2 K at 300 L/h, reflecting the expected enhancement in convective heat transfer due to increased *Re* and reduced thermal boundary layer thickness in internal flows (Incropera et al. 2007; White 2011). The numerical model accurately reproduces this trend across the full operating range. For water, the results show good agreement with experimental data, with deviations of approximately within ±10–15% for the investigated flow rates, indicating acceptable accuracy within typical uncertainty bounds for RANS-based simulations (Wilcox 2006; Duangthongsuk and Wongwises 2010). The slight overprediction at low flow rates is consistent with known limitations of eddy-viscosity turbulence models in transitional regimes. For the nanofluids, the h is consistently higher than that of water at all flow rates. At 100 L h^{-1}, the experimental h increases from 850 W/m K (water) to 1000 W/m K (0.04%) and 1150 W/m K (0.25%), corresponding to enhancements of approximately 17.6% and 35.3%,

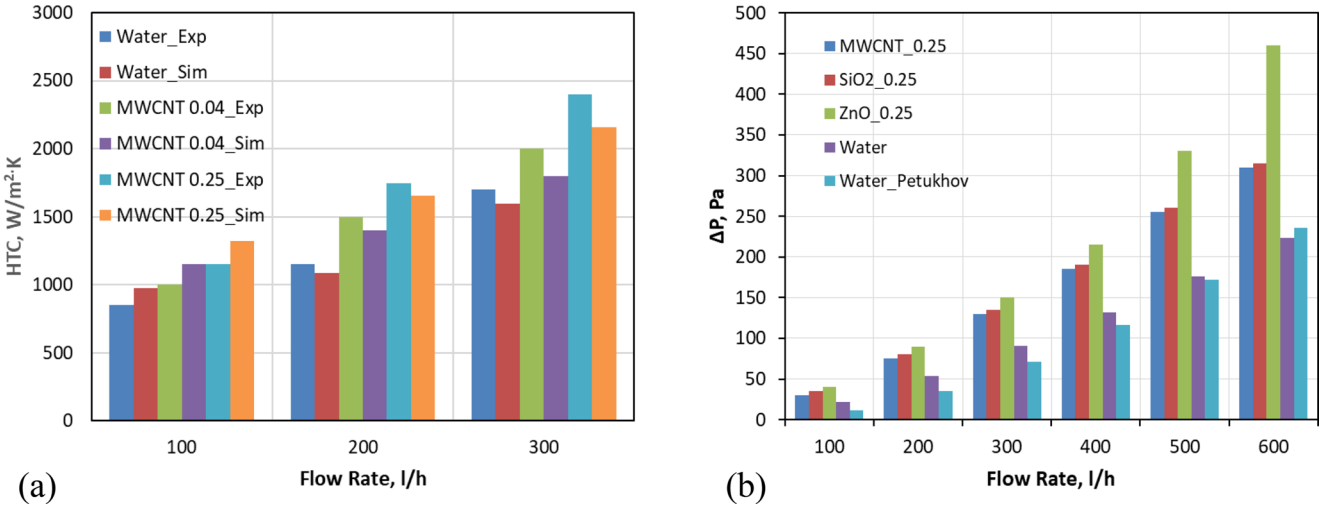

Fig. 4 (**a**) Comparison of experimental vs numerical h for water and MWCNT nanofluids (0.04% and 0.25%), (**b**) ΔP comparison for water and nanofluids at 0.25% concentration, including benchmark against the Petukhov smooth-pipe correlation

respectively. At 300 L/h, the h reaches 2000 W/m K (0.04%) and 2400 W/m K (0.25%), representing enhancements of 17.6% and 41.2% relative to water. These values are consistent with experimentally reported enhancement ranges for dilute nanofluids in internal flows (Pak and Cho 1998; Xuan and Li 2003; Duangthongsuk and Wongwises 2010; Mahian et al. 2017). The numerical results capture both the magnitude and concentration-dependent factor of h. Predicted enhancements follow the same ordering (0.04% <0.25%) and closely match experimental ratios, with deviations generally within ±10–15% for the h values. This demonstrates that the model accurately reproduces the underlying thermophysical mechanisms governing nanofluid heat transfer. The discrepancies observed at the lowest and highest flow rates are systematic across all fluids, suggesting a global modelling bias (e.g., turbulence closure or inlet conditions). Therefore, the agreement between h and the enhancement confirms the robustness of numerical models for dilute nanofluid flows in double-pipe heat exchangers.

To assess hydraulic consistency, the CFD-predicted pressure drop for water was benchmarked against the Darcy–Weisbach relation using the Petukhov smooth-pipe correlation (Eqs. 19 and 20) (Petukhov 1970; Incropera et al. 2007), as shown in Fig. 4b.

$$\Delta P = f\frac{L}{D}\frac{\rho \mathrm{U}^2}{2} \tag{19}$$

The Darcy friction factor for smooth turbulent pipe flow was evaluated using the Petukhov correlation (Petukhov 1970).

$$f = (0.79\mathrm{In}Re - 1.64)^{-2} \tag{20}$$

Good agreement was obtained in both magnitude and trend, particularly at moderate and high flow rates, confirming that the numerical model correctly captures the baseline internal-flow resistance. Building on this validated baseline, the 0.25% nanofluid cases for MWCNT, SiO_2, and ZnO were directly compared with water (Fig. 4b). All nanofluids exhibited higher pressure drops than water, with the magnitude of the ΔP penalty increasing systematically with nanofluid type and effective viscosity. This demonstrates that the model reproduces the expected hydraulic scaling of dilute nanofluid flows without relying solely on temperature-based validation.

While direct experimental validation data are available for water and MWCNT nanofluids (Moradi et al. 2019), the extension to SiO_2 and ZnO nanofluids is supported by the fact that the governing transport mechanisms remain identical and are fully captured through the effective thermophysical properties (ρ, μ, k, Cp). The numerical framework resolves the same Navier–Stokes and energy equations for all fluids, with differences arising only from property variations. Furthermore, the predicted thermo-hydraulic trends for SiO_2 and ZnO (e.g., monotonic increase of ΔP with μ and enhancement of q'' with k) are consistent with established experimental observations for oxide nanofluids in internal flows. Therefore, although direct experimental datasets for all nanofluids are not available, the validated model demonstrates mechanistic consistency and predictive transferability across nanofluid types within the dilute regime ($\phi \leq 0.25\%$).

3.2 Thermophysical model justification

The selection of thermophysical property models in the present study is consistent with both classical theory and

contemporary nanofluid literature. The Einstein (Eq. 3) and Maxwell (Eq. 4) formulations are well established for dilute suspensions and remain widely used as baseline models due to their analytical consistency and robustness at low nanoparticle volume fractions. For viscosity, comparisons are made with advanced formulations that account for particle interactions: the Brinkman (Eq. 21) and Batchelor (Eq. 22) models. A comparative evaluation was performed at the maximum nanoparticle concentration (ϕ=0.25%).

$$\mu_{nf} = \mu_{bf}(1-\phi)^{-2.5} \tag{21}$$

$$\mu_{nf} = \mu_{bf}\left(1 + 2.5\phi + 6.2\phi^2\right) \tag{22}$$

For thermal conductivity, comparison is made with the Hamilton–Crosser model (Eq. 23), which accounts for particle shape effects through a sphericity-dependent factor (Hamilton and Crosser 1962) and the Yu–Choi model (Eq. 24), which incorporates interfacial layer effects (Yu and Choi 2003):

$$k_{nf} = k_{bf} \times \frac{k_p + (\mathrm{n}-1)\,k_{bf} - (\mathrm{n}-1)\,\phi\,(k_{bf} - k_p)}{kp + (\mathrm{n}-1)\,k_{bf} + \phi\,(k_{bf} - k_p)} \tag{23}$$

Where $n = \frac{3}{\psi}$ is the shape factor. For MWCNT that is highly non-spherical (cylindrical/fibrous), $\psi \ll 1$, which implies that $n \gg 3$. Therefore, Eq. 23 is evaluated with a spherical approximation due to a dilute region (shape effects are second-order), therefore, $n = 3$. The Yu–Choi model (Eq. 24) is defined as:

$$k_{nf} = k_{bf} \times \frac{k_{pe} + 2k_{bf} + 2\phi\,(k_{pe} - k_{bf})}{\mathrm{kpe} + 2k_{bf} - \phi\,(k_{pe} - k_{bf})} \tag{24}$$

Where the effective particle conductivity k_{pe} is defined as:

$$k_{pe} = k_p\left(\frac{r_p + \delta}{r_p}\right)^3 \tag{25}$$

Table 3 Comparison of viscosity and thermal conductivity models at $\phi = 0.25\%$

	Viscosity
Model	$\frac{\mu_{nf}}{\mu_{bf}}$
Einstein (Eq. 3),	1.00625
Brinkman (Eq. 21)	1.00630
Batchelor (Eq. 22)	1.00629
	Thermal Conductivity
	$\frac{k_{nf}}{k_{bf}}$
Maxwell (Eq. 4)	1.0073
Hamilton-Crosser (Eq. 23)	1.0073
Yu-Choi (Eq. 24)	1.0073

Equation 24 extends the classical Maxwell formulation (Eq. 4) by incorporating an interfacial nanolayer around nanoparticles, thereby increasing the effective particle conductivity and enhancing heat transfer. However, for dilute concentrations ($\phi \leq 0.25\%$) and negligible interfacial thickness ($\delta \to 0$), this effect becomes insignificant, and Eqs. 4 and 24 converge, yielding identical predictions (Yu and Choi 2003).

The comparative analysis (Table 3) shows that at the maximum concentration considered (φ ≤0.25%), all models yield virtually identical thermophysical properties, with deviations of less than 0.01% for viscosity and 0.002% for thermal conductivity. This behaviour is consistent with established literature demonstrating that classical models remain valid for dilute nanofluids, while deviations from more advanced correlations become significant only at higher concentrations (Khanafer and Vafai 2011; Mahian et al. 2019). Accordingly, higher-order corrections do not introduce any meaningful change in the predicted thermo-hydraulic behaviour in the present regime, thereby validating the use of classical effective-property models without loss of accuracy.

3.3 Uncertainty analysis

The uncertainty associated with the numerical simulations was assessed using a root-sum-square (RSS) propagation applied to the primary derived quantities, including q'', h , ΔP, and PEC. The analysis combines contributions from discretisation sensitivity, turbulence model sensitivity, and validation deviation, and should therefore be interpreted as model-form and numerical uncertainty, rather than a strict measurement-based uncertainty. The convective heat transfer coefficient (h) is defined in Eq. 13 and its relative uncertainty is expressed as:

$$\left(\frac{U_h}{h}\right)^2 = \left(\frac{U_{q''}}{q''}\right)^2 + \left(\frac{U_{\Delta T_{lm}}}{\Delta T_{lm}}\right)^2 \tag{26}$$

The uncertainty related to Nu is expressed as:

$$\left(\frac{U_{Nu}}{Nu}\right)^2 = \left(\frac{U_h}{h}\right)^2 + \left(\frac{U_k}{k}\right)^2 \tag{27}$$

The ΔP uncertainty is estimated from its sensitivity to numerical resolution and turbulence modelling. Based on mesh refinement and model comparison, the relative uncertainty in ΔP is estimated to be within ±7%.

For PEC (Eq. 16), the corresponding propagated uncertainty is expressed as:

$$\left(\frac{U_{PEC}}{PEC}\right)^2 = \left(\frac{U_{q''/q''_0}}{q''/q''_0}\right)^2 + \left(\frac{1}{3}\frac{U_{\Delta P/\Delta P_0}}{\Delta P/\Delta P_0}\right)^2 \quad (28)$$

The exponent $1/3$ reduces the sensitivity of PEC to hydraulic uncertainty, so that thermal contributions remain dominant.

Mesh independence was verified through grid refinement, with variations in key flow variables remaining below 0.5%. Turbulence model sensitivity was assessed by comparing the realizable k-ε model with higher-fidelity approaches (LES/SAS), yielding deviations of approximately 5–7% in thermal and flow fields. In addition, validation against experimental data showed deviations in heat-transfer quantities within ±10–15%, which is taken here as a conservative estimate of overall model-form uncertainty. Combining these contributions using RSS yields an estimated uncertainty of approximately ±15% for absolute thermal quantities such as $q''$and h, dominated by validation deviation. For normalised quantities and performance metrics (e.g., q''/q''_0, $\Delta P/\Delta P_0$, and PEC), partial cancellation of systematic modelling errors is expected due to the consistent numerical framework applied across all cases. As a result, the effective uncertainty in these relative metrics is expected to be lower than that of the corresponding absolute quantities, although a conservative bound of the same order is retained. Therefore, the uncertainty analysis confirms that while absolute thermo-hydraulic quantities are subject to an estimated uncertainty of approximately ±15%, the use of normalised performance metrics reduces the impact of systematic errors. This provides a reliable basis for comparative evaluation, particularly for assessing thermo-hydraulic performance using dimensionless ratios and performance criteria introduced in the subsequent sections.

4 Results and discussion

4.1 Effect of flow rate on heat transfer

Nanofluids of MWCNT, SiO_2, and ZnO were used as the inner-tube working fluids in separate simulation cases at 0.04% concentration to examine the effect of flow rate on heat transfer performance. Figure 5 shows the heat transfer behaviour of the three nanofluids across flow rates ranging from 100 to 600 l/h, in terms of both the h and q''. In Fig. 5a, the h initially decreases from 100 to 200 l/h and then increases monotonically with increasing flow rate, reflecting the transition from low-velocity dominance to enhanced convective transport at high velocities. The slight reduction between 100 and 200 l/h reflects the dependence of the calculated heat-transfer coefficient on the log-mean temperature difference (ΔT_{lm}) used in its evaluation. As the flow rate increases, the fluid velocity rises, leading to a transition from laminar to turbulent flow. This transition reduces the thickness of the thermal boundary layer at the tube wall, increases fluid mixing, and enhances convective heat transfer. The higher q'' observed at higher flow rates (Fig. 5b), therefore reflecting more efficient thermal transport and correspondingly higher h. Under turbulent flow, turbulent eddies continuously disrupt the boundary layer and transport hotter core fluid toward the wall, further increasing convective heat transfer. Among the nanofluids considered, ZnO exhibits the highest thermal performance at higher flow rates. This trend is consistent with that of Shahrul et al. (2016), who reported that ZnO nanofluids exhibit greater heat transfer enhancement potential than SiO_2 nanofluids. However, excessively high flow rates increase pumping power requirements, leading to diminishing overall efficiency gains.

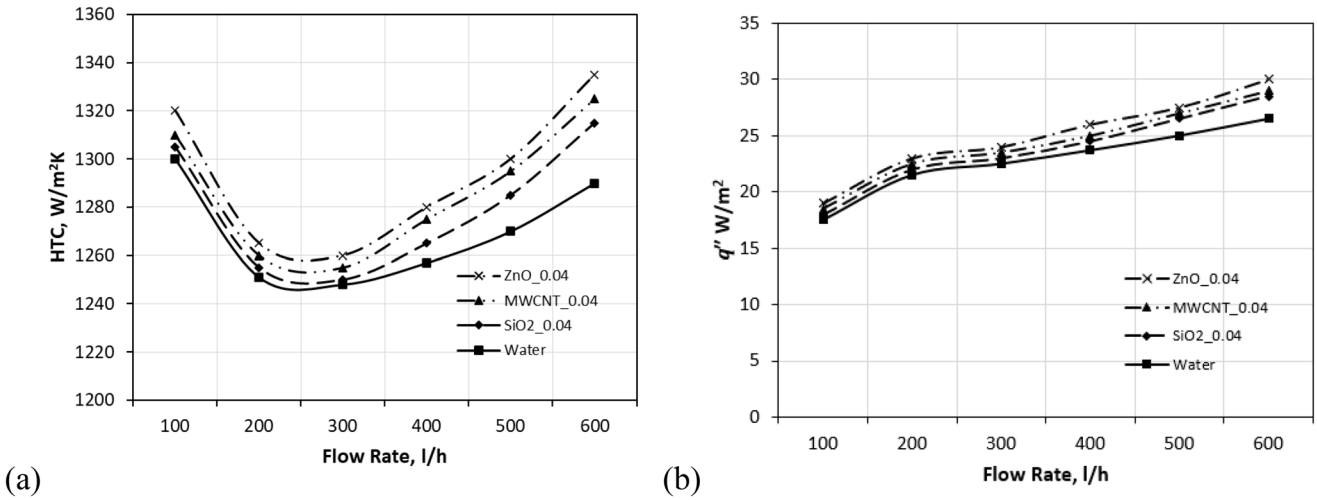

Fig. 5 Effect of flow rate at 0.04% nanofluid concentration (**a**) h (**b**) heat flux (q'')

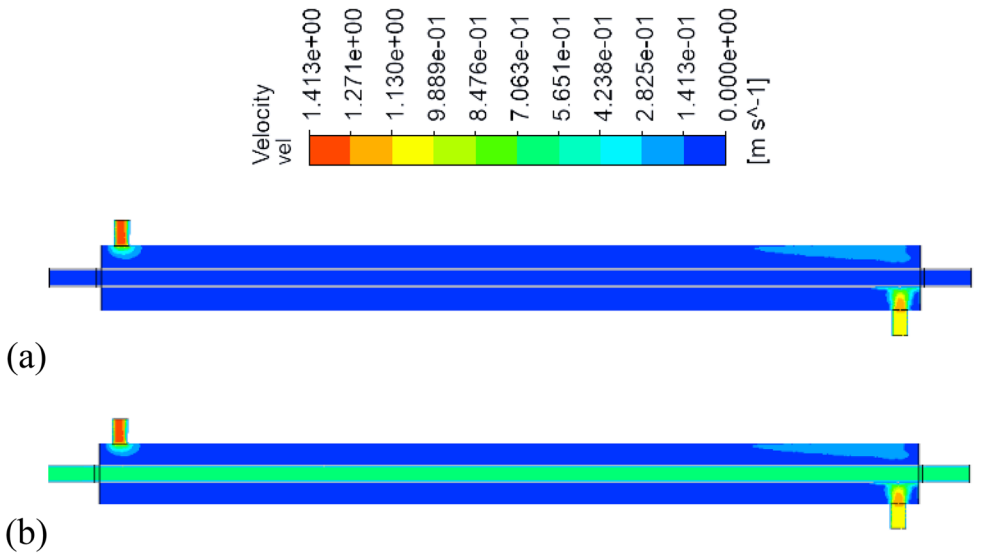

Fig. 6 Velocity contours (**a**)100 l/h (**b**) 600 l/h

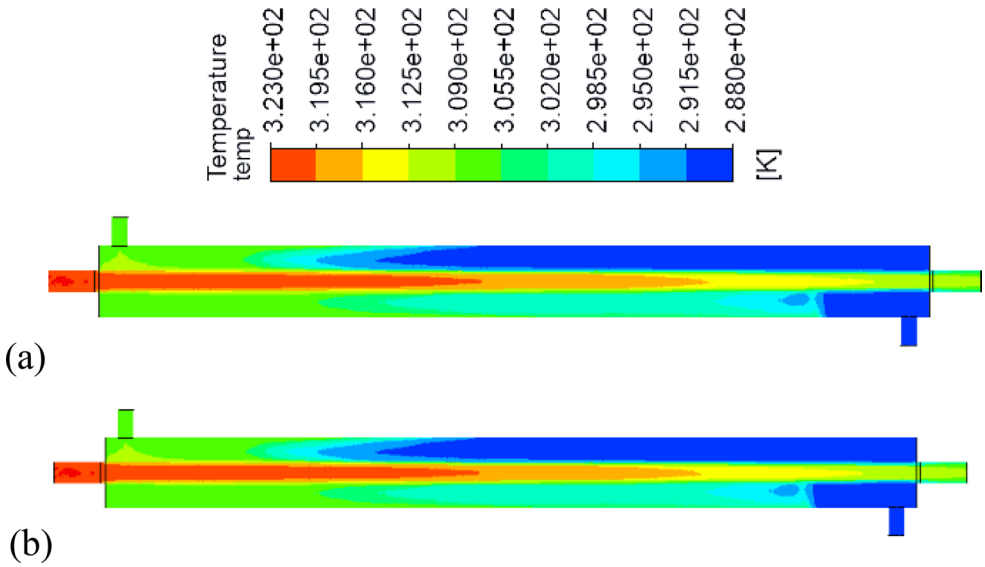

Fig. 7 Temperature contours at 0.25%, 50 °C, (**a**)100 l/h (**b**) 600 l/h

The contours in Figs. 6 and 7 illustrate the velocity and temperature distributions along the heat exchanger for all three nanofluids at a mass concentration of 0.25%. The profiles reveal the influence of varying flow rates on thermal and hydrodynamic behaviour. Results are shown for inlet volumetric flow rates of 100 l/h and 600 l/h in the inner tube. At the lower flow rate (100 l/h), the fluid exhibits weaker mixing and thicker thermal boundary layers, characteristic of transitional flow, even though the corresponding *Re* lies near the lower bound of the transitional regime (White 2011). Under these conditions, turbulence is not yet fully developed, resulting in slower mixing and reduced convective heat transfer to the shell side. In contrast, the 600 l/h case produces noticeably higher temperatures at the shell outlet. The velocity field shows the onset of turbulent or transitional behaviour, enhancing mixing within the tube and thinning the thermal boundary layer. This results in a more effective heat transfer mechanism and higher overall thermal performance. These observations suggest that, for applications requiring efficient heat dissipation, higher flow rates, such as 600 l/h, provide significantly improved heat transfer compared to low-flow, laminar operating conditions.

4.2 Effect of nanofluid concentration

Mass concentrations of 0.04%, 0.17%, and 0.25% were used to determine the thermophysical properties of the MWCNT, ZnO, and SiO_2 nanofluids. Figure 8 illustrates the variation of the q'' with flow rate for water and water-based MWCNT, SiO_2 and ZnO nanofluids at different concentrations. Across all subfigures, q'' increases monotonically with increasing flow rate, indicating enhanced convective heat transfer due to higher fluid velocity and improved thermal

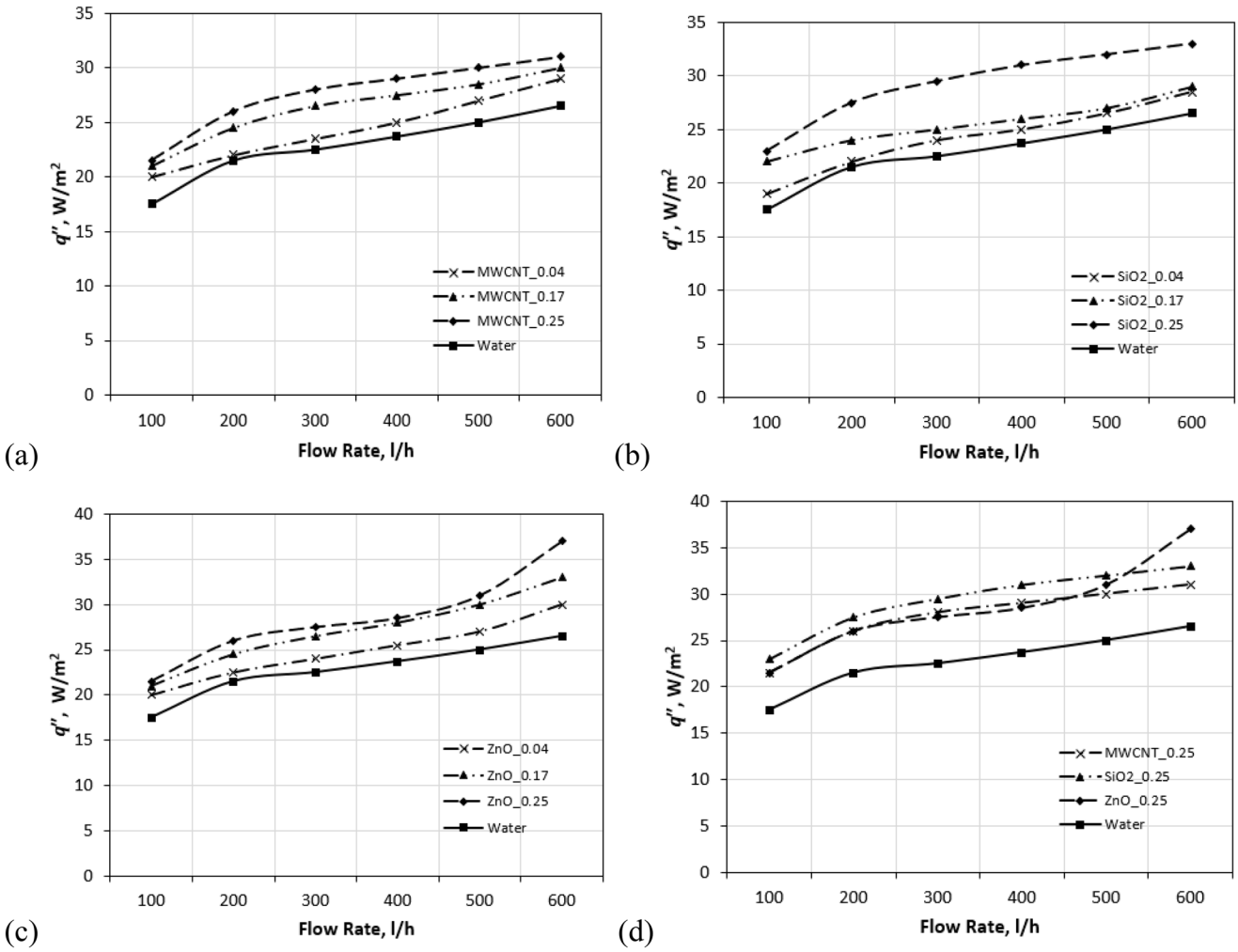

Fig. 8 Effect of nanofluid concentration on q'' (**a**) MWCNT (**b**) SiO_2 (**c**) ZnO (**d**) all nanofluids at 0.25% concentration

mixing. This trend is consistent with the expected increase in Re and turbulence intensity at higher flow rates. For the MWCNT nanofluid (Fig. 8a), the q''increases with nanoparticle concentration at all flow rates. The 0.25% concentration exhibits the highest q'', followed by 0.17% and 0.04%, while water consistently shows the lowest performance. The enhancement becomes more pronounced at higher flow rates, suggesting a synergistic effect between increased turbulence and the superior thermal conductivity of MWCNT nanoparticles. Figure 8b shows a similar trend for SiO_2. The addition of nanoparticles leads to a noticeable improvement in heat transfer compared to water, with higher concentrations yielding greater q''. However, the overall enhancement for SiO_2 is less pronounced than that observed for MWCNT, which can be attributed to the comparatively lower thermal conductivity of SiO_2 nanoparticles. In the case of ZnO (Fig. 8c), a significant increase in q'' is observed with increasing concentration and flow rate. At 0.25% concentration, ZnO demonstrates the highest q'' among the individual nanofluids, particularly at higher flow rates. This behaviour is associated with the combined effects of elevated thermal conductivity and improved energy transport mechanisms within the nanofluid. Figure 8d compares all nanofluids at a fixed concentration of 0.25%. Under identical operating conditions, ZnO exhibits the highest q'', followed by SiO_2 and MWCNT, while water remains the least effective. At higher flow rates, ZnO surpasses SiO_2 in heat-transfer rate, indicating improved performance under high-velocity conditions. This comparison highlights the strong influence of nanoparticle material properties on convective heat transfer performance. This quantitative decomposition reveals a fundamental mechanistic distinction based on particle morphology. The MWCNT enhancement is primarily conductivity-driven because its tubular, high-aspect-ratio structure promotes a percolating thermal network. Conversely, ZnO performance is governed by inertia-driven convective transport, where its higher density increases fluid momentum and advective transport. This suggests that the optimal

nanofluid choice depends on whether the regime favours diffusive (shape-based) or advective (mass-based) transport mechanisms. These results highlight non-linear behaviour, indicating that higher nanoparticle concentrations do not always yield proportional heat-transfer enhancement and that optimal concentration depends on both nanofluid type and flow rate.

To further clarify these trends, particularly the role of thermophysical normalisation, Figure 9 shows the variation in the Nusselt number (Nu) with Re for water-based MWCNT, SiO_2 and ZnO nanofluids at different concentrations. For all nanofluids and concentrations, Nu increases monotonically with Re, reflecting enhanced convective heat transfer with increasing flow velocity and turbulence intensity. At a given Re, however, Nu decreases slightly with increasing nanoparticle concentration, with 0.04% consistently yielding the highest *Nu* and 0.25% the lowest. At a given *Re*, *Nu* decreases slightly with increasing nanoparticle concentration despite an increase in h. This behaviour arises from the thermophysical normalisation inherent in Nu definition (Eq. 15). Although nanoparticle addition increases the heat-transfer coefficient, the effective thermal conductivity of the nanofluid increases more rapidly, leading to a slight reduction in the ratio *h/k* and, consequently, lower Nu values. Among the individual nanofluids, MWCNT and ZnO exhibit comparable Nu values, while SiO_2 shows slightly higher Nu over the investigated range of Re. The comparative plot at 0.25% confirms that SiO_2 yields the highest Nu, followed by MWCNT and ZnO. These results indicate that although nanoparticle addition enhances the heat-transfer coefficient, the dimensionless Nu remains primarily governed by the Re and Pr within the single-phase effective-property consideration.

The temperature profiles in Fig. 10 show progressively higher shell-side outlet temperatures as nanoparticle concentration increases from 0.04% to 0.25%, demonstrating the strong influence of nanoparticle loading on heat exchanger performance. This trend is consistent across all three nanofluids examined: MWCNT, SiO_2, and ZnO. A higher shell outlet temperature indicates greater heat transfer from the

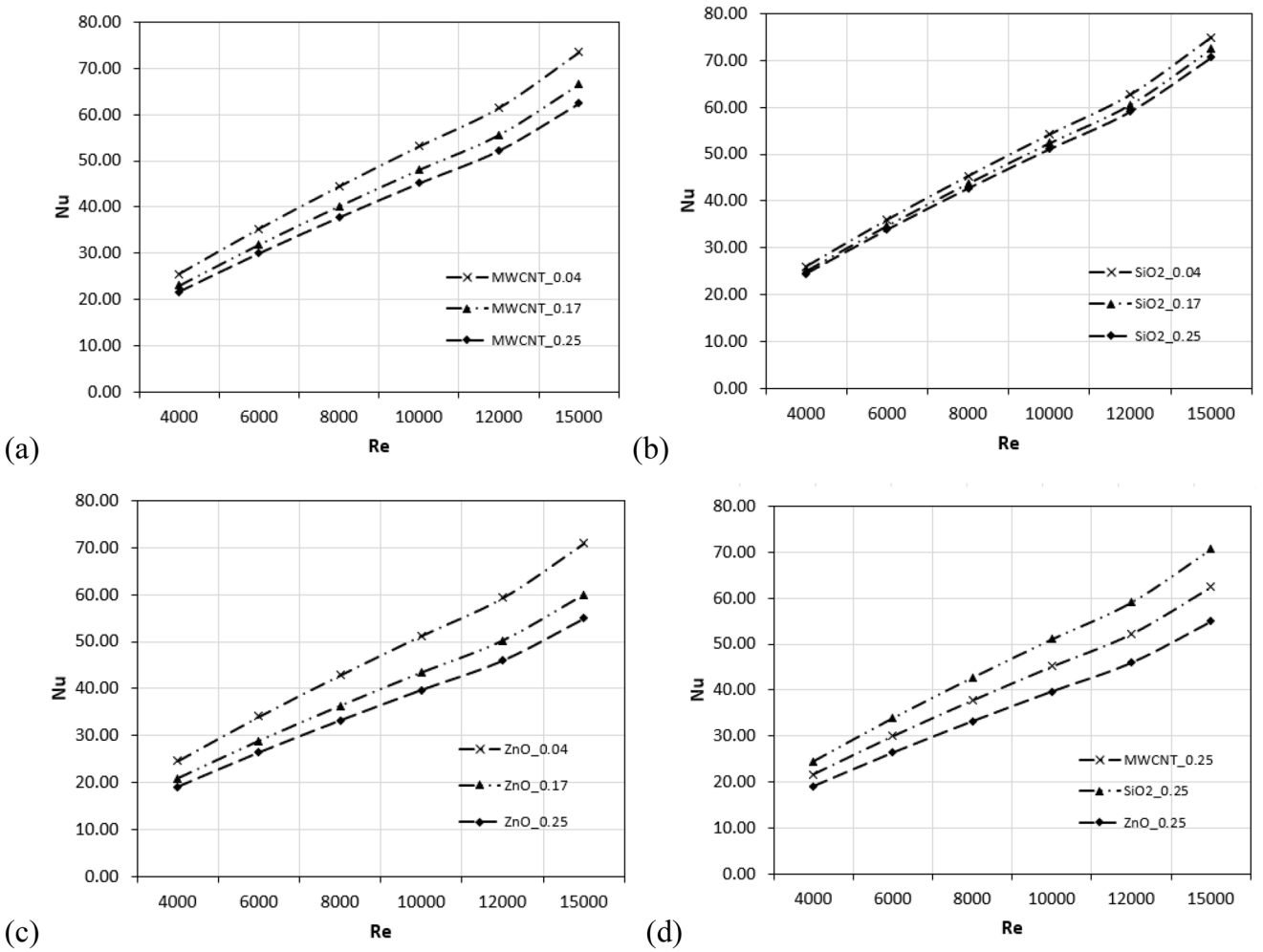

Fig. 9 Effect of nanofluid concentration on *Nu* (**a**) MWCNT (**b**) SiO_2 (**c**) ZnO (**d**) all nanofluids at 0.25% concentration

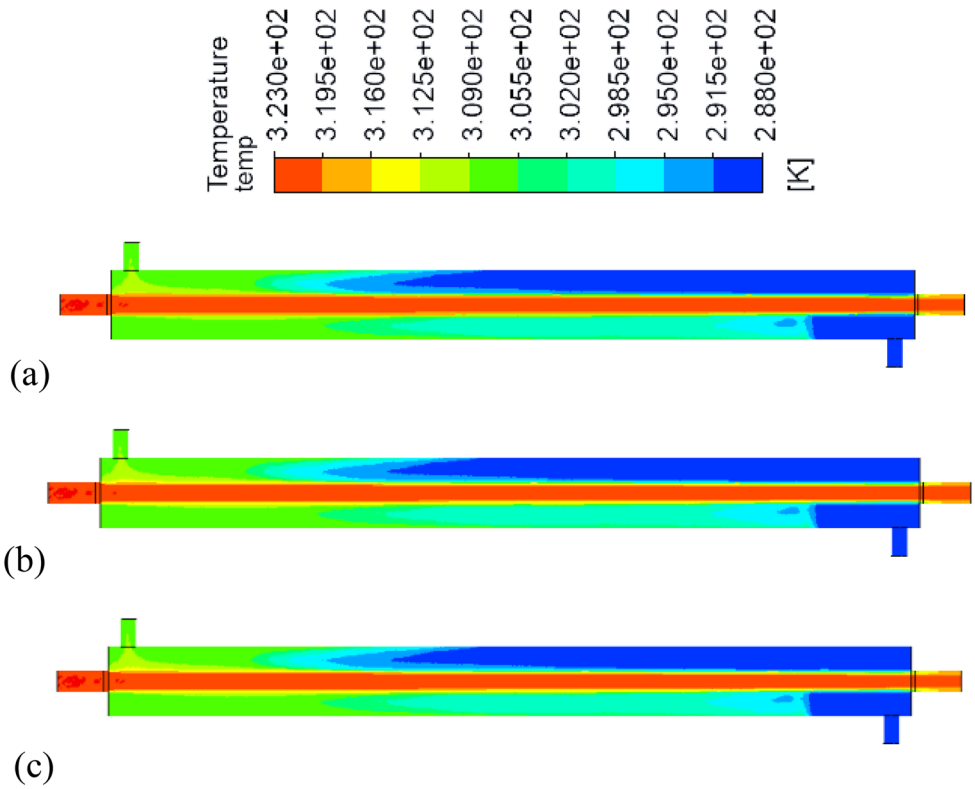

Fig. 10 Temperature contours at 600 l/h, 50 °C (**a**) 0.04%, (**b**) 0.17%, (**c**) 0.25%

tube-side fluid, as the effective thermal conductivity of the working fluid increases with nanoparticle loading. Consequently, the 0.25% concentration level enhances thermal performance by promoting stronger convective heat transfer, thereby improving the overall heat exchanger performance.

The combined effects of flow rate and nanoparticle concentration can be further interpreted through classical scaling in internal flows. Within the present range ($Re = 3.4 \times 10^3 - 2.05 \times 10^4$), the flow spans transitional to fully turbulent regimes, where convective heat transfer is governed by inertial–diffusive interactions and near-wall mixing. This behaviour follows the classical scaling law $Nu \propto Re^{0.8} Pr^{0.4}$ for turbulent internal flow. The transition from Re = 3,400 to Re = 20,500 shifts the system into a fully turbulent regime where convective transport dominates. Mechanistically, this transition facilitates thinning of the boundary layer. According to scaling theory, the thermal boundary layer thickness scales as $\delta_t \sim L \cdot Re^{-1/5}$, such that increasing Re leads to a thinner near-wall thermal resistance layer. At higher flow rates (e.g., 600 l/h), the reduced boundary-layer thickness enhances fluid mixing and heat transfer by increasing the wall temperature gradient. The addition of nanoparticles modifies this scaling behaviour by altering effective thermophysical properties: increased thermal conductivity promotes energy diffusion, while increased viscosity influences both Re and turbulence structure. These competing effects explain the observed enhancement in heat transfer with increasing concentration, along with the associated thermo-hydraulic trade-off.

4.3 Pressure drop analysis

While Sect. 4.2 established the thermal scaling governing heat transfer enhancement, the corresponding hydraulic behaviour is governed by momentum transport mechanisms, which are examined here. Figures 11a–11c present the ΔP behaviour of MWCNT, SiO_2, and ZnO nanofluids at increasing flow rates and concentrations. Across all nanofluids, the ΔP increases monotonically with flow rate, consistent with the rise in axial velocity and corresponding frictional losses along the inner tube. At a fixed nanoparticle concentration, higher flow rates intensify wall shear, leading to higher Darcy friction factors and, consequently, larger ΔP s (White 2011). For each nanofluid type, the ΔP increases with particle concentration due to the associated rise in effective viscosity. This hydraulic penalty is a direct consequence of enhanced momentum diffusion. The increased effective viscosity (μ_{nf}) creates a steeper velocity gradient at the tube wall, increasing the wall shear stress (τ_w), defined by $\tau_w = \mu_{nf} \left(\frac{du}{dy} \right)_{y=0}$. For high-density particles like ZnO, momentum loss scales more aggressively than thermal gain at high concentrations, leading to the observed decline in the PEC. The presence of nanoparticles alters the fluid's microstructure and enhances momentum diffusion,

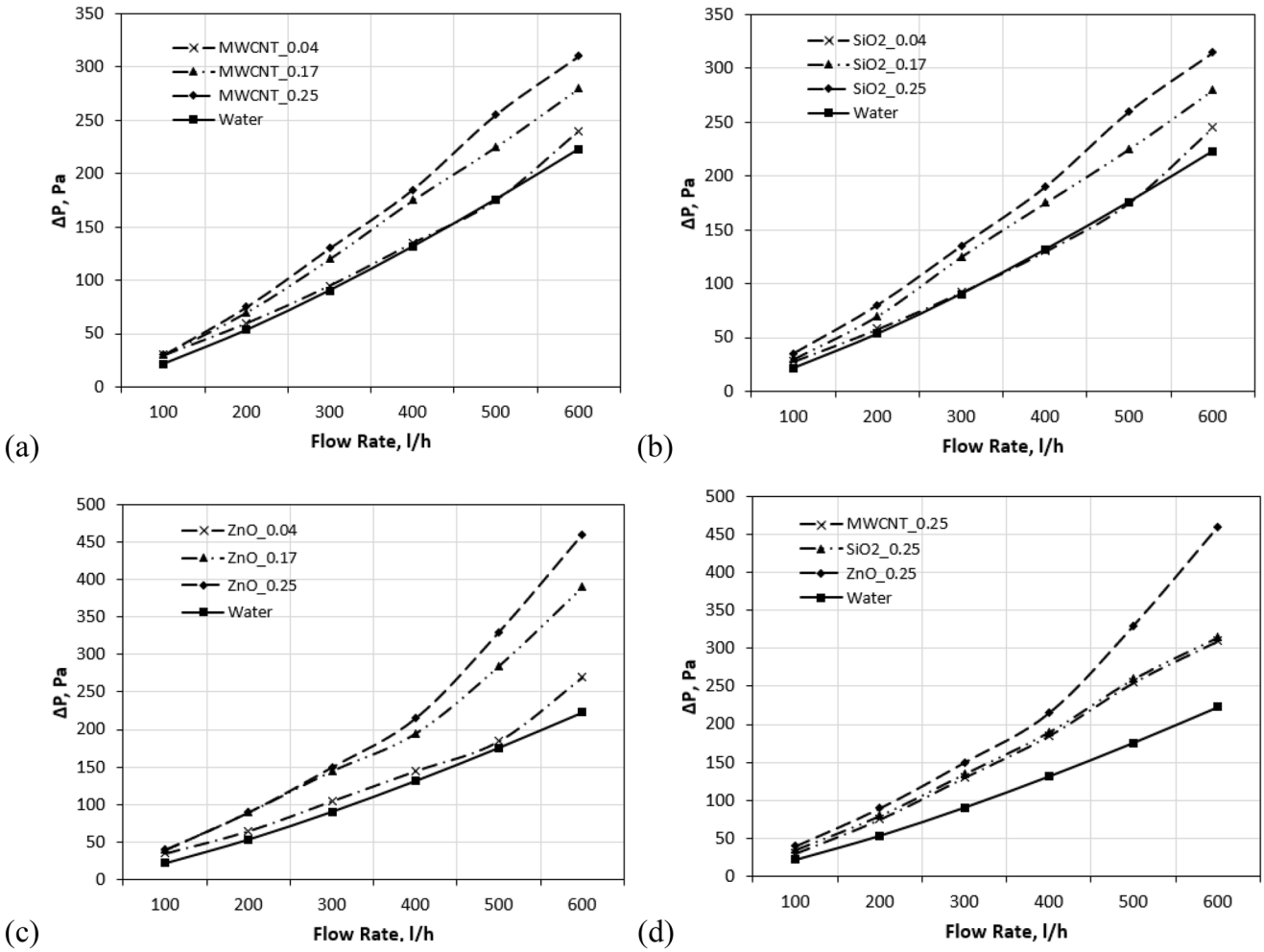

Fig. 11 Pressure drop (ΔP) (**a**) MWCNT (**b**) SiO_2 (**c**) ZnO (**d**) All nanofluids at 0.25% concentration

thereby increasing the fluid's resistance to flow. Among the three nanofluids, ZnO exhibits the highest ΔP, most notably at 500 and 600 l/h (Fig. 11c). The higher pressure drop observed for ZnO is primarily associated with the increase in effective viscosity, which enhances wall shear stress and frictional losses, while density variations contribute secondarily through the dynamic pressure term. This behaviour can be attributed to ZnO's comparatively higher viscosity contribution and a greater tendency for particle clustering at higher shear rates. Although not explicitly modelled, particle aggregation may contribute to the observed pressure drop trends. If aggregation occurs, it may increase the effective viscosity of the nanofluid beyond that predicted by the dilute-suspension model, potentially leading to a higher pressure drop penalty than reported here.

Consequently, the present model may slightly underestimate the hydraulic cost associated with ZnO, although the qualitative trend of higher pressure losses relative to MWCNT and SiO_2 would remain unchanged. However, within the scope of the present CFD model, the pressure increase can be attributed to changes in effective thermophysical properties. Figure 11d directly compares the three nanofluids at 0.25% concentration and shows that ZnO consistently produces the largest ΔP, followed by MWCNT and SiO_2. This ranking correlates with the relative increases in effective viscosity introduced by each nanoparticle type. These findings underscore an important design consideration: although nanofluids enhance heat transfer, their use also increases ΔP, especially at higher concentrations and flow rates, thereby increasing pumping power requirements (Abdelrazek et al. 2018; Mahian et al. 2017). Therefore, an optimal balance between thermal performance and hydraulic penalty must be considered when integrating nanofluids into heat exchanger systems. The observed thermo-hydraulic trade-off can be interpreted through near-wall transport mechanisms. In internal flow, pressure drop is governed by wall shear stress arising from velocity gradients at the wall, while heat transfer is controlled by the development of the thermal boundary layer. Increasing the Reynolds number increases both wall shear stress (increasing ΔP) and

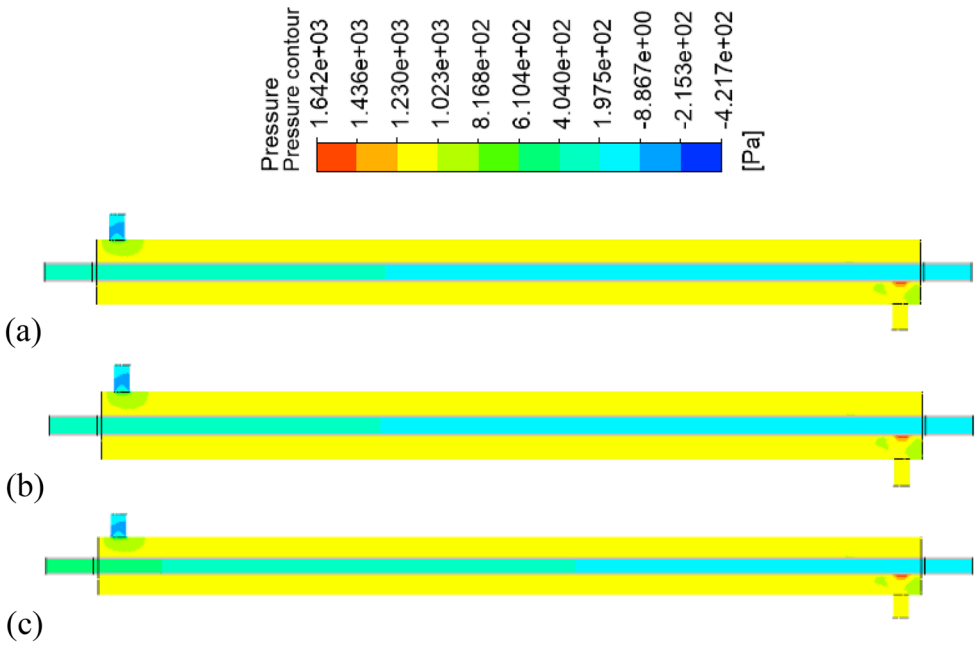

Fig. 12 Pressure contours at 600 l/h, 0.25%, 70 °C (**a**) MWCNT, (**b**) SiO_2, (**c**) ZnO

turbulence intensity, promoting near-wall mixing and reducing the thermal boundary-layer thickness, thereby enhancing heat transfer. The addition of nanoparticles modifies this coupling by increasing viscosity (raising wall shear and ΔP) and enhancing thermal conductivity (improving heat diffusion), explaining the concurrent increase in hydraulic penalty and thermal performance. While ΔP was used as an indirect indicator of flow resistance in this study, the spatial distribution of wall shear stress was not evaluated. Wall shear stress mapping would provide deeper insight into local frictional behaviour, particularly in regions of accelerating flow or turbulence transition. This omission represents a limitation of the present analysis. Future work will therefore incorporate detailed wall shear stress predictions to inform surface optimisation strategies and evaluate fouling potential, which is often influenced by local shear conditions.

Building on these findings, Fig. 12 shows that the entry region of the inner tube differs among the three nanofluids, even though their overall pressure contours appear broadly similar. Notably, the ZnO exhibits a much higher pressure and a smoother pressure transition than the MWCNT and SiO_2 nanofluids. These differences indicate variations in fluid dynamics arising from the distinct thermophysical properties of each nanofluid, particularly viscosity and particle dispersion behaviour. The high pressure observed for the ZnO suggests that, at a 0.25% mass concentration, it experiences greater flow resistance. This increased resistance reflects the influence of a higher effective viscosity, leading to greater frictional losses and a more pronounced ΔP along the tube.

In Fig. 13, the combined %ΔP–flow-rate plot shows that pressure-drop penalties are primarily governed by

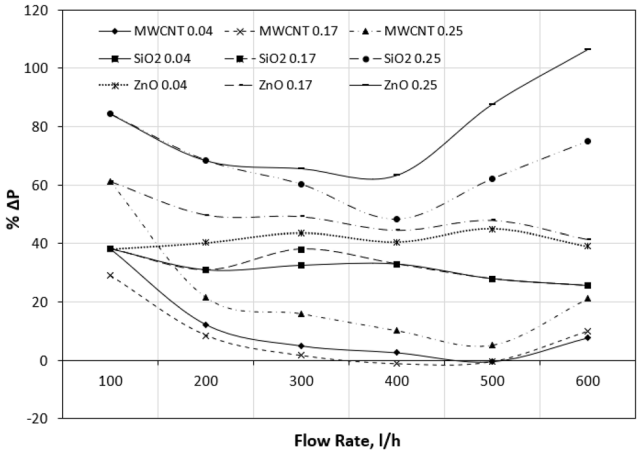

Fig. 13 Percentage pressure-drop relative to water for nanofluids at 0.04%, 0.17%, and 0.25% concentrations

nanoparticle concentration and secondarily by nanofluid type. The percentage pressure drop relative to water is defined as: $\%\Delta P = [(\Delta P_{nf} - \Delta P_{water})/\Delta P_{water}] \times 100$. At 0.04% concentration, all nanofluids impose only minor hydraulic penalties, with MWCNT and SiO_2 remaining close to the water baseline across most of the flow range, while ZnO consistently exhibits higher pressure losses. Increasing the concentration to 0.17% results in a marked increase in ΔP, with MWCNT and SiO_2 showing similar behaviour, while ZnO shows a substantially larger penalty at all flow rates. At 0.25%, the separation between nanofluids becomes pronounced: ZnO exhibits the largest hydraulic penalty, exceeding a 100% increase relative to water at high flow rates, consistent with the higher effective viscosity associated with the increased nanoparticle concentration, whereas

MWCNT and SiO_2 exhibit more moderate increases of approximately 40%. The percentage differences appear larger at low flow rates due to small baseline values and should therefore be interpreted cautiously. Overall, the results indicate that pressure-drop penalties increase nonlinearly with concentration and are strongly material-dependent, with ZnO presenting the least favourable hydraulic performance and MWCNT the most hydraulically benign behaviour. It should be noted that these pressure-drop trends were obtained from grid-independent CFD solutions using temperature-dependent thermophysical properties and therefore reflect the intrinsic hydraulic behaviour associated with the effective viscosity increase of the nanofluids.

4.4 Quantitative thermo-hydraulic decomposition

To quantitatively resolve the relative contributions of thermophysical properties and flow effects, the thermo-hydraulic response was decomposed using the governing definitions introduced in Sects. 2.6 and 3.1 For thermal response, Eqs. 13 and 15 are combined to give the tube-side heat flux expressed as:

$$q'' = \frac{Nuk}{D}\Delta T_{lm} \tag{29}$$

At identical operating conditions, Eq. 29 yields the heat flux enhancement (q''_{nf}/q''_{bf}) written as:

$$\frac{q''_{nf}}{q''_{bf}} = \frac{Nu_{nf}}{Nu_{bf}} \cdot \frac{k_{nf}}{k_{bf}} \cdot \frac{\Delta T_{lm,nf}}{\Delta T_{lm,bf}} \tag{30}$$

This formulation (Eq. 30) separates the thermal response into a convective contribution (Nu_{nf}/Nu_{bf}), a conductivity contribution (k_{nf}/k_{bf}), and thermal-driving-force contribution ($\Delta T_{lm,nf}/\Delta T_{lm,bf}$).

Similarly, the hydraulic response was decomposed using Eq. 19, which gives (at fixed operating conditions) the following expression:

$$\frac{\Delta P_{nf}}{\Delta P_{bf}} = \frac{\rho_{nf}}{\rho_{bf}} \cdot \frac{f_{nf}}{f_{bf}}, Re \propto \frac{\rho U}{\mu} \tag{31}$$

This expression (Eq. 31) gives the direct density contribution through ρ_{nf}/ρ_{bf}, while the friction-factor ratio (f_{nf}/f_{bf}) captures the combined influence of viscosity and Re on the observed hydraulic behaviour.

Figure 14 shows the quantitative decomposition, providing direct insight into the mechanisms governing the thermohydraulic performance at 600 l/h and 0.25% nanofluid concentration. For thermal response, Figure 14a shows the relative contributions, indicating that the *Nu* accounts for approximately 23–30%, 27–32%, and 19–23% for MWCNT, SiO_2, and ZnO, respectively. In contrast, thermal conductivity contributes about 43–48%, 33–36%, and 27–30%, while the thermal-driving-force contribution increases to 28–32%, 38–41%, and 48–52%, respectively. This demonstrates a clear shift in dominant mechanisms, from conductivity-driven enhancement (MWCNT) to thermal-driving-force-dominated behaviour (ZnO), explaining why ZnO achieves the highest heat-flux enhancement despite a reduced *Nu*. For the hydraulic decomposition, the corresponding contributions (Fig. 14b) show that density accounts for approximately 47–49% (MWCNT and SiO_2) and 41–43% (ZnO), while the friction-factor contribution increases from 51 to 53% to 57–59% for ZnO. This confirms that the hydraulic penalty is primarily governed by frictional effects rather than density alone, particularly at higher nanoparticle influence.

Importantly, both thermal and hydraulic responses are fundamentally governed by the Re, which couples density, velocity, and viscosity. At a fixed flow rate, increases in effective viscosity reduce Re, leading to elevated friction-factor contributions and suppressed convective transport (lower Nu). This is evident in the present results, where fluids exhibiting higher friction-factor contributions simultaneously show reduced *Nu* contributions. In contrast, density variations contribute directly to the inertial component of ΔP but have a comparatively smaller influence on the overall hydraulic response. The observed behaviour therefore reflects a coupled viscosity–flow interaction, in which viscosity governs the modification of the flow regime through Re, while density primarily influences the magnitude of the inertial effect.

The combined response (Fig. 14c) reflects the balance between these competing mechanisms. ZnO exhibits the highest heat-flux enhancement $\left(q''_{nf}/q''_{bf}=1.396\right)$ but also incurs the largest ΔP penalty ($\Delta P_{nf}/\Delta P_{bf}=2.063$), consistent with its strong thermal-driving-force contribution and dominant frictional penalty. In contrast, SiO_2 achieves a more balanced thermo-hydraulic performance due to a more even distribution of thermal contributions and a relatively moderate friction-factor increase. These results confirm that optimal thermo-hydraulic performance arises from a balance between conductivity-driven heat-transfer enhancement and viscosity-driven hydraulic losses, rather than maximising any single component.

4.5 Effect of temperature

The temperature field analysis is presented for the highest concentration (0.25%) and flow rate (600 l/h) investigated, as these conditions produce the most pronounced thermal

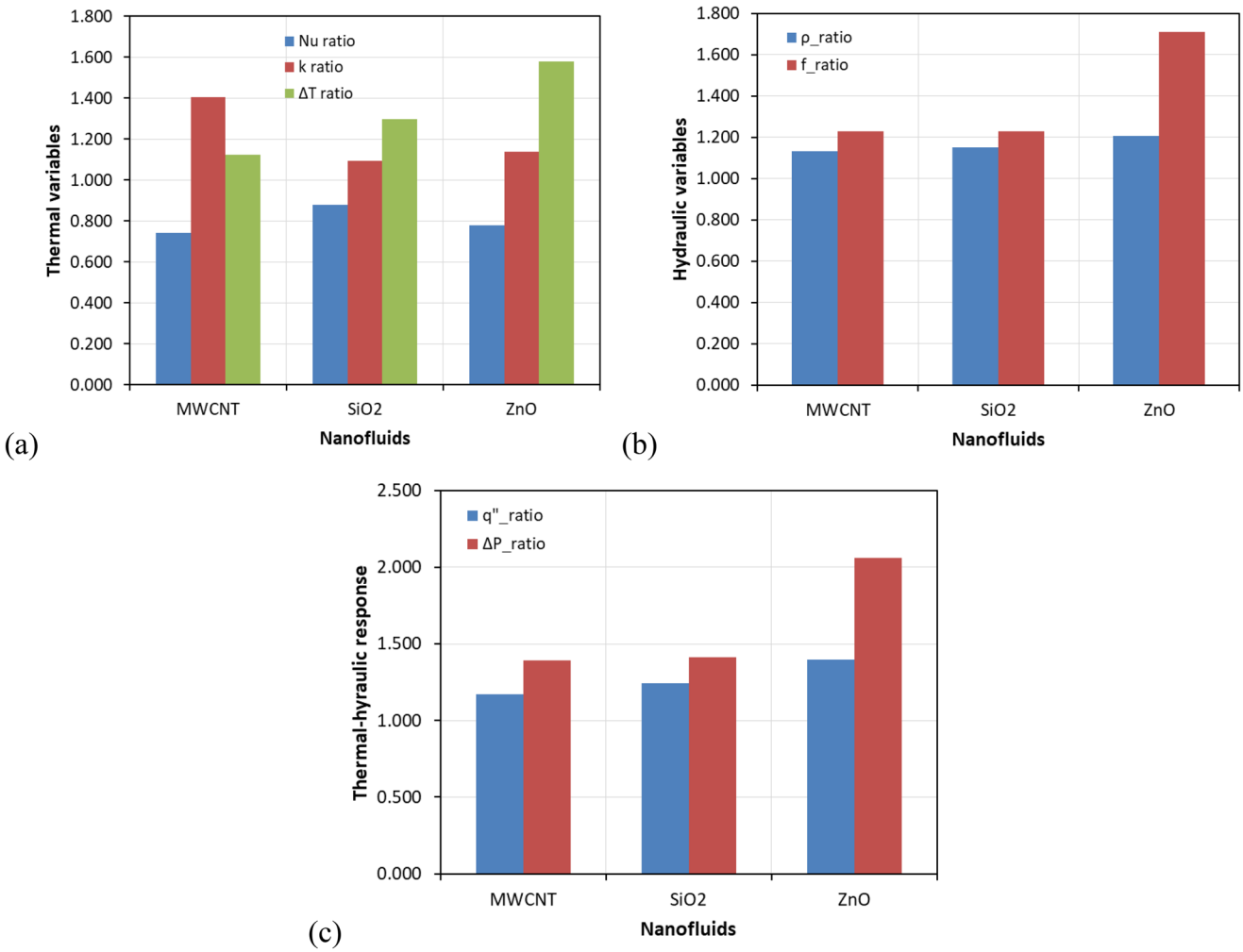

Fig. 14 Quantitative thermo-hydraulic decomposition at 600 l/h and 0.25% (**a**) relative contributions of convective transport (Nu_{nf}/Nu_{bf}), thermal conductivity (k_{nf}/K_{bf}), and thermal-driving-force ($\Delta T_{lm,nf}/\Delta_{lm,bf}$) to heat-flux enhancement, (**b**) relative contributions of density (p_{nf}/p_{bf}) and friction-factor (f_{nf}/f_{bf}) to ΔP. (**c**) Heat-flux enhancement (q''_{nf}/q''_{bf}) and ΔP penalty ($\Delta P_{nf}\Delta P_{bf}$)

response and provide a representative comparison of the nanofluids' temperature behaviour. As shown in Fig. 15, increasing the inlet temperature leads to a corresponding rise in the q'' for all three nanofluids. The results indicate that higher turbulence enhances fluid-tube surface interaction, reducing the thermal boundary layer and improving both the h and the q''. Raising the inlet temperature increases the temperature gradient across the fluid, thereby enhancing thermal energy transport. Higher temperatures also reduce fluid viscosity, improving flow behaviour and lowering hydraulic resistance. This reduction in viscosity increases flow momentum and decreases the ΔP across the heat exchanger. In addition, increased temperatures reduce the thermal resistance between the fluid and the tube wall, enabling more effective heat transfer. However, excessively high temperatures may introduce material or operational limitations. Therefore, optimising temperature, flow rate, and *Re* is essential to balancing heat transfer performance, ΔP, and pumping power. within the scope of the present numerical model (Fig. 14), ZnO exhibits the highest numerically predicted heat-transfer enhancement across the investigated temperature range at 600 L/h and 0.25% concentration. It should be noted that the increase in heat flux with inlet temperature corresponds to a proportional increase in the h and the Nu, since these quantities are derived from the same thermal field (cf. Eqs. 12 and 14). The comparative behaviour among nanofluids remains consistent. ZnO exhibits the strongest temperature sensitivity due to its higher effective thermal conductivity, followed by MWCNT and SiO_2. The effect of flow rate on the flow regime as a function of temperature is shown in Fig. 15b.

The temperature contours in Fig. 16 illustrate the thermal behaviour of the heat exchanger for all three nanofluids considered. As the inner-tube inlet temperature increases from

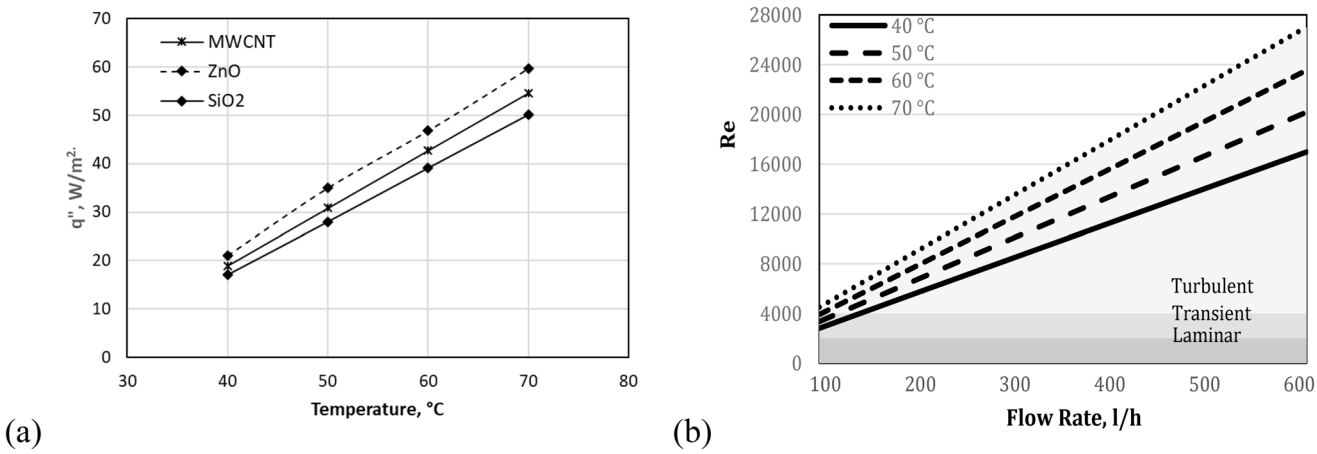

Fig. 15 Effect of temperature (**a**) q'' vs temperatures at 600 L/h and 0.25% (**b**) flow regime for different flow rates and temperatures

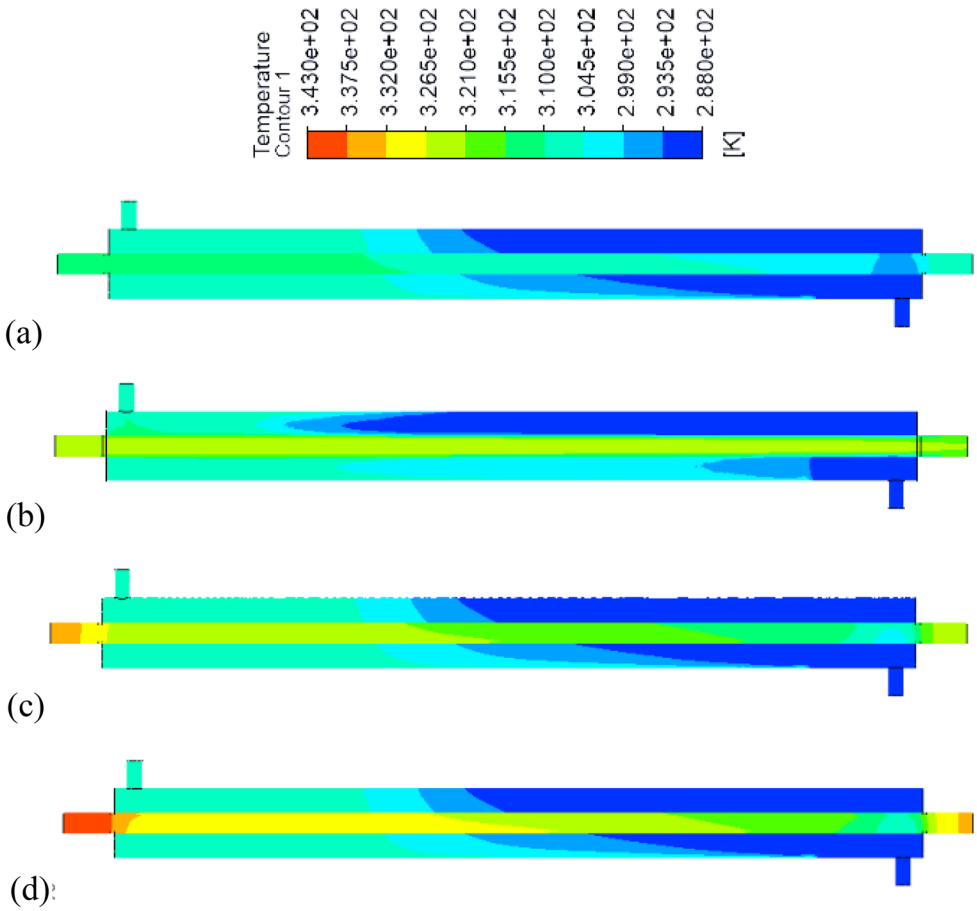

Fig. 16 Temperature contours at 600 l/h at 0.25% concentration (**a**) 40 °C, (**b**) 50 °C, (**c**) 60 °C, (**d**) 70 °C

40 °C to 70 °C, the shell-side outlet temperature rises, demonstrating enhanced heat transfer at higher inlet temperatures. The slightly elevated contour temperature observed at 50 °C reflects a non-linear interaction between temperature-dependent viscosity reduction, enhanced convective mixing, and fluid residence time. At higher temperatures, increased flow momentum marginally reduces local thermal accumulation despite overall heat-transfer enhancement. These findings highlight the importance of optimising flow rate, inlet temperature, and Re to achieve maximum heat transfer effectiveness in nanofluid-based heat exchangers. The efficiency of modern heat exchanger designs depends on fully utilising the improved thermophysical properties of nanofluids while operating within the turbulent flow regime

To assess the generality of the results with respect to operating temperature, the heat flux of each nanofluid was

normalised by the base fluid at the corresponding temperature. Figure 17(a–b) shows that the normalised heat flux (q''^{nf}/q''^{bf}) remains nearly invariant across 40–70 °C, with relative variations limited to approximately 1–5%, indicating weak temperature sensitivity. MWCNT and SiO_2 exhibit highly stable behaviour (1.72% and 1.89%, respectively), while ZnO shows the highest enhancement (mean = 1.29) with a slightly larger yet still limited variation of 4.66%. All nanofluids maintain $q''^{nf}/q''^{bf} \geq 1$ across the full temperature range, confirming sustained thermal enhancement relative to water. Importantly, the performance ranking remains invariant (ZnO > MWCNT > SiO_2), with no crossover observed. This limited variation, relative to the overall enhancement magnitude, indicates that the thermo-hydraulic behaviour is primarily governed by *Re–Pr* scaling rather than by temperature. Physically, temperature affects all fluids through similar scaling of thermophysical properties (μ, k, Cp), while relative differences are dictated by concentration-dependent property ratios. Consequently, temperature modifies absolute heat transfer but does not alter relative performance, and the observed trends are representative of the broader operating envelope within the investigated *Re* and temperature ranges.

4.6 Performance evaluation criterion (PEC)

Figure 18 illustrates the variation of the performance evaluation criterion (PEC) with flow rate and nanoparticle concentration. As shown in Fig. 18(a), PEC generally increases with flow rate for all nanofluids, indicating greater heat-transfer enhancement at higher velocities. At low concentration (0.04%), PEC values remain close to unity across the investigated flow range, corresponding to modest net gains of approximately 3–6% relative to water at 600 l/h. As the concentration increases to 0.17%, PEC exhibits non-monotonic behaviour due to the competing effects of enhanced heat transfer and increased ΔP. SiO_2 show a slight reduction in PEC (−2%), indicating that the hydraulic penalty marginally outweighs the thermal enhancement under this condition. The concentrations considered here represent discrete points within the dilute nanofluid regime (0.04–0.25%). Although intermediate concentrations were not explicitly investigated, the observed PEC behaviour indicates that thermohydraulic performance within this range is governed by the balance between enhanced thermal conductivity and increasing hydraulic resistance. The absence of a similar PEC reduction at 0.04% can be attributed to the minimal increase in viscosity at this loading level. At 0.04%, the hydraulic penalty remains negligible, and even modest thermal conductivity enhancement is sufficient to maintain PEC values close to or slightly above unity. In contrast, at 0.17%, the increase in effective viscosity results in a disproportionate rise in pressure drop that is not fully offset by the incremental heat-transfer gain, leading to a temporary reduction in PEC. At 0.25% (Fig. 18 (b)), however, the stronger enhancement in thermal conductivity restores the balance, and the heat-transfer gains outweigh the hydraulic penalty. This behaviour highlights the nonlinear coupling between nanoparticle loading and thermo-hydraulic performance. The concentrations considered here represent discrete points within the dilute nanofluid regime (0.04–0.25%). Although intermediate concentrations between 0.17% and 0.25% were not explicitly simulated, the observed non-monotonic PEC response demonstrates that thermo-hydraulic optimisation within this regime is governed by the competing effects of thermal enhancement and hydraulic penalty. Therefore, additional intermediate points would refine the exact optimum but are not expected to alter the comparative conclusions or nanofluid ranking reported here.

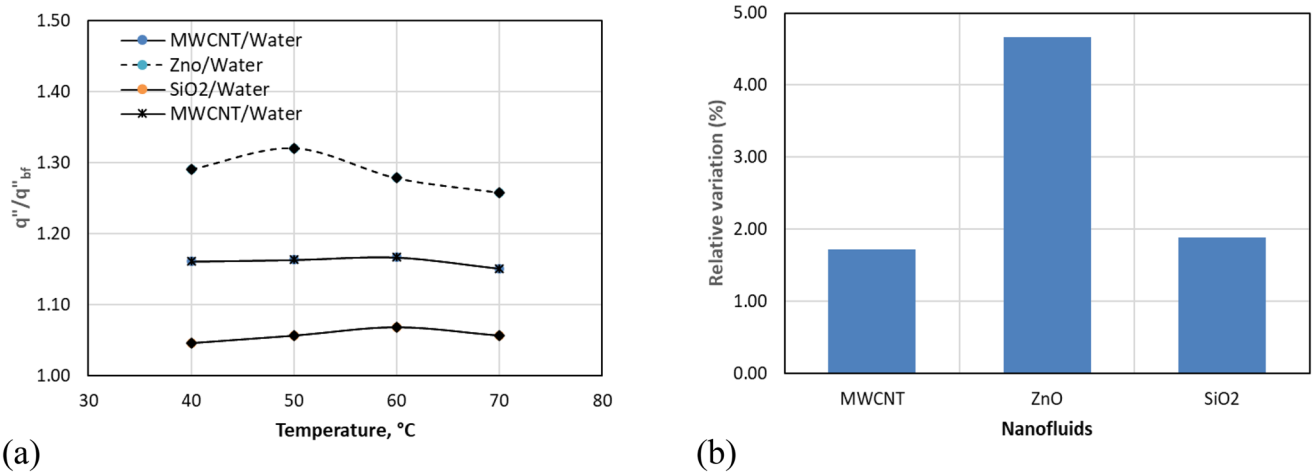

Fig. 17 (**a**) Normalised heat flux q''^{nf}/q''^{bf} as a function of temperature (40–70 °C) at 0.25% concentration and 600 l/h (**b**) Corresponding relative variation (%) of the q''^{nf}/q''^{bf}

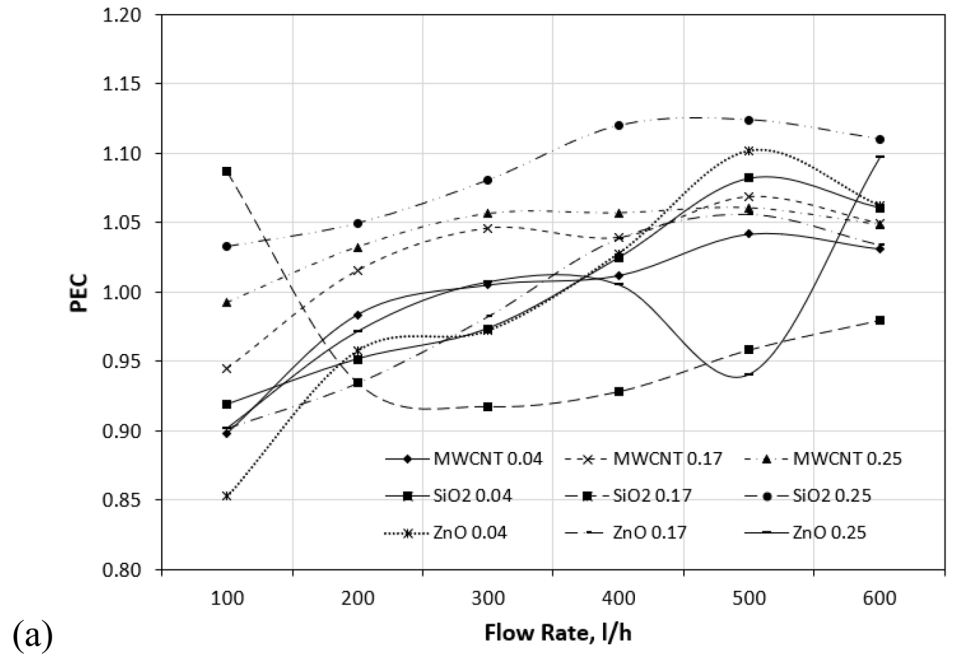

(a)

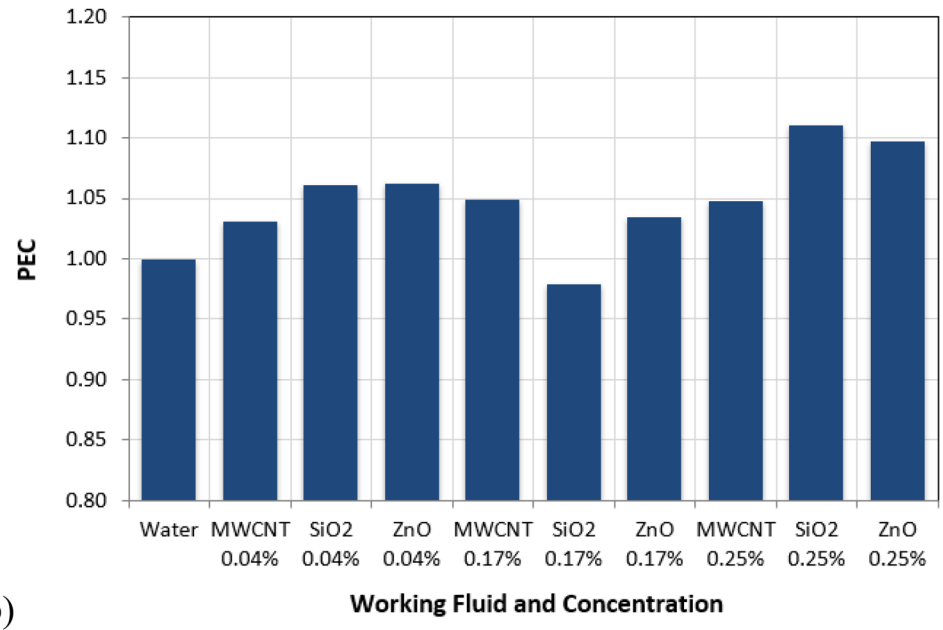

(b)

Fig. 18 PEC variations for all nanofluids and concentrations (**a**) 100–600 l/h flow rate (**b**) PEC at 600 l/h, relative to water

At 0.25% concentration, PEC improvements become more pronounced, reaching approximately 5% for MWCNT, 10% for ZnO, and up to 11% for SiO_2, which achieves the highest PEC among the investigated cases. Although MWCNT nanoparticles possess higher intrinsic thermal conductivity, thermo-hydraulic performance is governed by the balance between heat-transfer enhancement and pressure-drop penalty. SiO_2 nanofluids provide a moderate increase in thermal conductivity while maintaining relatively lower viscosity and density than ZnO and MWCNT nanofluids, resulting in a more favourable trade-off between thermal enhancement and hydraulic losses under the examined operating conditions. The concentrations investigated (0.04–0.25%) represent discrete points within the dilute nanofluid regime. Although intermediate values could refine the optimal value, the thermohydraulic response varies smoothly and monotonically with concentration. Consequently, the optimum at 0.25% (particularly for SiO_2) reflects a robust trend rather than an isolated point. Therefore, PEC analysis confirms that SiO_2 provides the most favourable thermo-hydraulic

performance, followed by MWCNT, while ZnO is limited by its disproportionately higher hydraulic cost.

In the context of the quantified uncertainty bounds (Sect. 3.3), these conclusions remain unaffected. While absolute values of heat transfer and pressure drop carry uncertainties of approximately ±15%, the comparative evaluation is based on normalised metrics (q''/q''_0, $\Delta P/\Delta P_0$, and PEC), for which systematic errors partially cancel due to the consistent numerical framework applied across all cases. As a result, the effective uncertainty in relative performance metrics is reduced. Importantly, the differences in PEC between the nanofluids exceed the estimated uncertainty bounds, ensuring that the observed performance ranking (SiO_2 >MWCNT >ZnO) remains invariant within the uncertainty range. This confirms that the identified optimum and overall thermo-hydraulic trends are robust and not sensitive to the quantified uncertainties.

5 Conclusion

This study presents a controlled, experimentally validated CFD comparison of MWCNT, SiO_2, and ZnO nanofluids in a double-tube heat exchanger under identical geometric and boundary conditions to isolate the intrinsic thermo-hydraulic behaviour. The results show that nanofluids enhance convective heat transfer relative to water but also increase pressure losses, confirming that heat-transfer enhancement alone does not ensure optimal performance. When thermal and hydraulic effects are evaluated using the performance evaluation criterion (PEC), SiO_2 nanofluid at 0.25% concentration and 600 L/h provides the most favourable balance, achieving an overall thermo-hydraulic improvement of approximately 11% compared with water, with the observed performance ranking remaining robust within the estimated uncertainty bounds. Although ZnO yields the highest absolute heat-transfer rates, its significantly higher pressure drop penalty limits its practical advantage, whereas MWCNT shows moderate enhancement with comparatively lower hydraulic resistance. These results highlight the importance of PEC-based evaluation in heat-exchanger design, demonstrating that balanced thermo-hydraulic optimisation should guide nanofluid selection rather than heat-transfer enhancement alone. The study reveals that nanofluid performance is fundamentally linked to flow regime transitions; the onset of turbulence acts as a catalyst, enabling the specific morphology of MWCNTs or the density of ZnO to overcome the inherent viscous resistance of the base fluid. Practical implementation will also depend on factors such as nanoparticle cost, dispersion stability, and potential fouling or sedimentation effects, which were beyond the scope of this study. The geometry-controlled comparison framework developed here addresses a key limitation in the existing literature, in which nanofluid type and heat-exchanger configuration are often varied simultaneously. It provides a consistent reference for future experimental validation and multiphase modelling of nanofluid-based thermal systems.

Acknowledgements The authors gratefully acknowledge the support of the Faculty of Computing, Engineering and the Built Environment (now the School of Architecture, Built Environment, Computing and Engineering) at Birmingham City University (BCU) for providing access to the HPC (Cluster 3) facility. Olusegun Ilori and Rasheed Ayoola acknowledge the PhD funding support through the BCU's Faculty Dean Scholarship Award.

Author contributions O.I - supervised and provided resources; S.I. - performed analysis and wrote the manuscript text; R.A. - supervised and edited the manuscript; J.O. - supervised and edited the manuscript; A.O. - supervised and edited the manuscript. All authors reviewed the manuscripts.

Funding The authors received no external funding for this work.

Data availability Data will be made available upon reasonable request.

Declarations

Ethics approval This study did not involve human participants or animals.

Competing interests The authors declare no competing interests.

References

Abdelrazek AH, Alawi OA, Kazi SN, Yusoff N, Oon CS, Ali HM (2018) A new approach to evaluate the impact of thermophysical properties of nanofluids on heat transfer and pressure drop. Int Commun Heat Mass Transf 95:161–170. https://doi.org/10.1016/j.icheatmasstransfer.2018.05.002

Afshari F, Sözen A, Khanlari A, Tuncer AD (2021) Heat transfer enhancement of a finned shell-and-tube heat exchanger using Fe2O3/water nanofluid. J Cent South Univ 28(11):3297–3309

Ahamed R, Salehin M, Ehsan MM (2024) Thermal-hydraulic performance and flow phenomenon evaluation of a curved trapezoidal corrugated channel with E-shaped baffles implementing hybrid nanofluid. Heliyon 10(7):e28698–e28698. https://doi.org/10.1016/j.heliyon.2024.e28698

Ahmad F, Mahmud S, Ehsan MM, Salehin M (2023) Numerical assessment of nanofluids in corrugated minichannels: flow phenomenon and advanced thermo-hydrodynamic analysis. Int J Multiling Thermofluids 20(2666):100449. https://doi.org/10.1016/j.ijft.2023.100449

Ahmadi MR, Toghraie D (2022) Numerical analysis of flow and heat transfer in a shell-and-tube heat exchanger in the gas recirculation cooling system of a diesel engine and the effect of nanofluid on its performance. J Therm Anal Calorim 147(7):4853–4871. https://doi.org/10.1007/s10973-021-10831-1

Ajeeb W, Murshed SMS (2022) Nanofluids in compact heat exchangers for thermal applications: a state-of-the-art review. Therm Sci Eng Prog 30:101276. https://doi.org/10.1016/j.tsep.2022.101276

Albojamal A, Vafai K (2017) Analysis of single phase, discrete and mixture models, in predicting nanofluid transport. Int J Heat Mass Transf 114:225–237. https://doi.org/10.1016/j.ijheatmasstransfer.2017.06.030

ANSYS (2023) ANSYS Fluent User's Guide. ANSYS Inc

Buongiorno J (2006) Convective transport in nanofluids. J Heat Transf 128(3):240–250. https://doi.org/10.1115/1.2150834

Chauhan PR, Kumar R (2018) A comprehensive review on heat transfer enhancement and pressure drop characteristics of nanofluid flow through micro-channels. Ann Chim Sci Mat 42(3):363–385. https://doi.org/10.3166/acsm.42.363-385

Duangthongsuk W, Wongwises S (2010) An experimental study on the heat transfer performance and pressure drop of TiO2-water nanofluids flowing under a turbulent flow regime. Int J Heat Mass Transf 53(1–3):334–344. https://doi.org/10.1016/j.ijheatmasstransfer.2009.09.024

Einstein A (1906) Eine neue Bestimmung der Moleküldimensionen. Annalen der Phys 324(2):289–306. https://doi.org/10.1002/andp.19063240204

Estupiñán-Campos J, Quitiaquez W, Nieto-Londoño C, Quitiaquez P (2024) Numerical simulation of the heat transfer Inside a shell and tube heat exchanger considering different variations in the geometric parameters of the design. Energies 17(3):691–691. https://doi.org/10.3390/en17030691

Gabir MM, Alkhafaji D (2021) Comprehensive review on double pipe heat exchanger techniques. J Phys Conf Ser 1973(1):012013. https://doi.org/10.1088/1742-6596/1973/1/012013

Girhe NB, Botewad SN, More CV, Kadam SB, Pawar PP, Kadam AB (2023) Development of water-based CuO, TiO2 and ZnO nanofluids and comparative study of thermal conductivity and viscosity. Pramana - J Phys 97(2). https://doi.org/10.1007/s12043-023-02546-9

Gupta M, Kumar R, Arora N, Kumar S, Dilbagi N (2016) Forced convective heat transfer of MWCNT/Water nanofluid under constant heat flux: an experimental investigation. Arab J Sci Eng 41(2):599–609. https://doi.org/10.1007/s13369-015-1699-5

Hamilton RL, Crosser OK (1962) Thermal conductivity of heterogeneous two-component systems. Ind Eng Chem Fund 1(3):187–191. https://doi.org/10.1021/i160003a005

Ilori OM, Jaworski AJ, Mao X (2018) Experimental and numerical investigations of thermal characteristics of heat exchangers in oscillatory flow. Appl Therm Eng 144:910–925. https://doi.org/10.1016/j.applthermaleng.2018.07.073

Incropera FP, DeWitt DP, Bergman TL, Lavine AS (2007) Fundamentals of heat and Mass transfer, 6th edn. Wiley, New York

Islam U, Mustakim A, Ahamed R, Salehin M, Ehsan MM (2024) Advanced thermo-hydraulic assessment of helical pipes with different shapes of jackets using single-phase and hybrid nanofluids. Int J Multiling Thermofluids 22:100628–100628. https://doi.org/10.1016/j.ijft.2024.100628

Kadivar M, Tormey D, McGranaghan G (2023) A comparison of RANS models used for CFD prediction of turbulent flow and heat transfer in rough and smooth channels. Int J Multiling Thermofluids 20:100399–100399. https://doi.org/10.1016/j.ijft.2023.100399

Khanafer K, Vafai K (2011) A critical synthesis of thermophysical characteristics of nanofluids. Int J Heat Mass Transf 54(19–20):4410–4428. https://doi.org/10.1016/j.ijheatmasstransfer.2011.04.048

Launder BE, Spalding DB (1974) The numerical computation of turbulent flows. Comput Methods Appl Mech Eng 3(2):269–289. https://doi.org/10.1016/0045-7825(74)90029-2

Ilori OM, Jaworski AJ, Mao X, Ismail OS (2021) Effects of edge shapes on thermal-fluid processes in oscillatory flows. Therm Sci Eng Prog 25:101004. https://doi.org/10.1016/j.tsep.2021.101004

Maghrabie HM, Mousa HM (2022) Thermal performance intensification of car Radiator using SiO2/Water and ZnO/Water nanofluids. J Therm Sci Eng Appl 14(3):034501. https://doi.org/10.1115/1.4051382

Maghrabie HM, Attalla M, Mohsen AAA (2021) Performance assessment of a shell and helically coiled tube heat exchanger with variable orientations utilizing different nanofluids. Appl Therm Eng 182:116013. https://doi.org/10.1016/j.applthermaleng.2020.116013

Mahian O, Kianifar A, Heris SZ, Wen D, Sahin AZ, Wongwises S (2017) Nanofluids effects on the evaporation rate in a solar still equipped with a heat exchanger. Nano Energy 36:134–155. https://doi.org/10.1016/j.nanoen.2017.04.025

Mahian O, Kolsi L, Amani M, Estellé P, Ahmadi G, Kleinstreuer C, Marshall JS, Siavashi M, Taylor RA, Niazmand H, Wongwises S, Hayat T, Kolanjiyil A, Kasaeian A, Pop I (2019) Recent advances in modeling and simulation of nanofluid flows - Part I: fundamentals and theory. Phys Rep 790:1–48. https://doi.org/10.1016/j.physrep.2018.11.004

Marzouk SA, Al-Sood MMA, El-Said EMS, Younes MM, El-Fakharany MK (2023) A comprehensive review of methods of heat transfer enhancement in shell and tube heat exchangers. J Therm Anal Calorim 148(15):7539–7578. https://doi.org/10.1007/s10973-023-12265-3

Moradi A, Toghraie D, Isfahani, Hosseinian A, Isfahani AHM (2019) An experimental study on MWCNT–water nanofluids flow and heat transfer in double-pipe heat exchanger using porous media. J Therm Anal Calorim 137(5):1797–1807. https://doi.org/10.1007/s10973-019-08076-0

Mustakim A, Islam U, Ahamed R, Salehin M, Ehsan MM (2024) Numerical assessment of advanced thermo-hydrodynamic characteristics of nanofluid Inside a helically featured straight pipe. Int J Multiling Thermofluids 21:100591–100591. https://doi.org/10.1016/j.ijft.2024.100591

Pak BC, Cho YI (1998) Hydrodynamic and heat transfer study of dispersed fluids with submicron metallic oxide particles. Exp Heat Transf 11(2):151–170. https://doi.org/10.1080/08916159808946559

Perumal S, Venkatraman V, Sivanraju R, Mekonnen A, Thanikodi S, Chinnappan R (2022) Effects of nanofluids on heat transfer characteristics in shell and tube heat exchanger. Therm Sci 26(2 Part A):835–841. https://doi.org/10.2298/TSCI200426076P

Petukhov BS (1970) Heat transfer and friction in turbulent pipe flow with variable physical properties. Adv Heat Transf 6:503–564

Porgar S, Oztop HF, Salehfekr S (2023) A comprehensive review on thermal conductivity and viscosity of nanofluids and their application in heat exchangers. J Mol Liq 386:122213. https://doi.org/10.1016/j.molliq.2023.122213

Prasad TR, Krishna KR, Sharma KV, Bhaskar CN (2022) Thermal performance of stable SiO_2 nanofluids and regression correlations to estimate their thermophysical properties. J Indian Chem Soc 99(6):100461–100461. https://doi.org/10.1016/j.jics.2022.100461

Qasim M, Sajid Kamran M, Ammar M, Ali Jamal M, Yasar Javaid M (2020) Heat transfer enhancement of an Automobile Engine Radiator using ZnO water base nanofluids. J Therm Sci 29(4):1010–1024. https://doi.org/10.1007/s11630-020-1263-9

Rasheed AH, Alias H, Salman SD (2021) Thermophysical properties for ZnO-Water Nanofluid: experimental study. MSF 1025:9–14. https://doi.org/10.4028/www.scientific.net/MSF.1025.9

Sam Solomon DP, Selladurai V, Krishnan AS (2022) Experimental analysis on performance assessment of a hybrid double cross flow tube arrangement in a shell and tube heat exchanger. J Mech Sci Technol 36(1):499–511. https://doi.org/10.1007/s12206-021-1247-z

Shahrul IM, Mahbubul IM, Saidur R, Sabri MFM (2016) Experimental investigation on Al2O3–W, SiO2–W and ZnO–W nanofluids and their application in a shell and tube heat exchanger. Int J Heat Mass Transf 97:547–558. https://doi.org/10.1016/j.ijheatmasstransfer.2016.02.016

Shirvan KM, Mamourian M, Esfahani JA (2019) Experimental study on thermal analysis of a novel shell and tube heat exchanger with corrugated tubes. J Therm Anal Calorim 138(2):1583–1606. https://doi.org/10.1007/s10973-019-08308-3

Vidhya R, Balakrishnan T, Kumar BS (2022) Investigation on thermophysical properties of zinc oxide nanofluid for heat transfer applications. In Materials Today Proceedings, vol 58. pp 789–794

Webb RL (1981) Performance evaluation criteria for use of enhanced heat transfer surfaces in heat exchanger design. Int J Heat Mass Transf 24(4):715–726. https://doi.org/10.1016/0017-9310(81)90015-6

Webb RL, Eckert ERG (1972) Application of rough surfaces to heat exchanger design. Int J Heat Mass Transf 15(9):1647–1658. https://doi.org/10.1016/0017-9310(72)90095-6

White FM (2011) Fluid Mechanics, 7th edn. McGraw-Hill, New York

Wilcox DC (2006) Turbulence modeling for CFD, 3rd edn. DCW Industries, Inc

Xuan Y, Li Q (2003) Investigation on convective heat transfer and flow features of nanofluids. J Heat Transf 125(1):151–155. https://doi.org/10.1115/1.1532008

Yu W, Choi SUS (2003) The role of interfacial layers in the enhanced thermal conductivity of nanofluids: a renovated Maxwell model. J Nanopart Res 5(1–2):167–171. https://doi.org/10.1023/A:1024438603801

Yuan Y, Cao J, Zhang Z, Xiao Z, Wang X (2024) Experimental and numerical simulation study of a novel double shell-passes multi-layer helically coiled tubes heat exchanger. Int J Heat Mass Transf 227:125497–125497. https://doi.org/10.1016/j.ijheatmasstransfer.2024.125497

Zhu X, Haglind F (2020) Computational fluid dynamics modeling of liquid–gas flow patterns and hydraulics in the cross-corrugated channel of a plate heat exchanger. Int J Multiphase Flow 122:103163. https://doi.org/10.1016/j.ijmultiphaseflow.2019.103163